RESEARCH ARTICLE

Key Points:
- As spring Arctic sea ice matures, carbon dioxide undersaturation develops
- Abiotic processes dominated inorganic carbon in upper ice and early in season
- Biotic processes controlled inorganic carbon in bottom ice and late in season

Correspondence to:
K. A. Brown,
kbrown@whoi.edu

Inorganic carbon system dynamics in landfast Arctic sea ice during the early-melt period

Kristina A. Brown[1,2], Lisa A. Miller[3], C. J. Mundy[4], Tim Papakyriakou[4], Roger Francois[1], Michel Gosselin[5], Gauthier Carnat[6], Kyle Swystun[4], and Philippe D. Tortell[1,7]

[1]Department of Earth, Ocean and Atmospheric Sciences, University of British Columbia, Vancouver, British Columbia, Canada, [2]Department of Marine Chemistry and Geochemistry, Woods Hole Oceanographic Institution, Woods Hole, Massachusetts, USA, [3]Fisheries and Oceans Canada, Institute of Ocean Sciences, Sidney, British Columbia, Canada, [4]Centre for Earth Observation Science, University of Manitoba, Winnipeg, Manitoba, Canada, [5]Institut des sciences de la mer de Rimouski, Université du Québec à Rimouski, Rimouski, Québec, Canada, [6]Laboratoire de Glaciologie, Université Libre de Bruxelles, Brussels, Belgium, [7]Department of Botany, University of British Columbia, Vancouver, British Columbia, Canada

Abstract We present the results of a 6 week time series of carbonate system and stable isotope measurements investigating the effects of sea ice on air-sea CO_2 exchange during the early melt period in the Canadian Arctic Archipelago. Our observations revealed significant changes in sea ice and sackhole brine carbonate system parameters that were associated with increasing temperatures and the buildup of chlorophyll *a* in bottom ice. The warming sea-ice column could be separated into distinct geochemical zones where biotic and abiotic processes exerted different influences on inorganic carbon and pCO_2 distributions. In the bottom ice, biological carbon uptake maintained undersaturated pCO_2 conditions throughout the time series, while pCO_2 was supersaturated in the upper ice. Low CO_2 permeability of the sea ice matrix and snow cover effectively impeded CO_2 efflux to the atmosphere, despite a strong pCO_2 gradient. Throughout the middle of the ice column, brine pCO_2 decreased significantly with time and was tightly controlled by solubility, as sea ice temperature and in situ melt dilution increased. Once the influence of melt dilution was accounted for, both $CaCO_3$ dissolution and seawater mixing were found to contribute alkalinity and dissolved inorganic carbon to brines, with the $CaCO_3$ contribution driving brine pCO_2 to values lower than predicted from melt-water dilution alone. This field study reveals a dynamic carbon system within the rapidly warming sea ice, prior to snow melt. We suggest that the early spring period drives the ice column toward pCO_2 undersaturation, contributing to a weak atmospheric CO_2 sink as the melt period advances.

1. Introduction

Sea ice plays an important role in polar marine biogeochemical cycles, particularly with respect to the transport and storage of climatologically active gases such as CO_2. As a semipermeable interface, the presence of sea ice acts to impede gas transfer between the surface ocean and the atmosphere. However a number of studies have documented direct sources or sinks of CO_2 across the sea ice-atmosphere interface at different times of year [e.g., *Semiletov et al.*, 2004; *Delille*, 2006; *Papakyriakou and Miller*, 2011], suggesting that the ice is not simply a passive barrier. Seasonal redistribution of inorganic carbon across the atmosphere-ice-ocean interface is coupled with the yearly freeze-melt cycle and driven by both abiotic and biotic processes. These processes include microbial activity (photosynthesis and respiration), brine concentration-dilution, calcium carbonate precipitation-dissolution, and inorganic carbon release to surface waters [e.g., *Rysgaard et al.*, 2009; *Arrigo et al.*, 2010; *Thomas et al.*, 2010; *Chierici et al.*, 2011; *Miller et al.*, 2011b]. The combination of such dynamic seasonal processes and heavy bias toward warm-period sampling has limited our understanding of the seasonal sea ice cycle's role in the polar carbon budget. Notably, comprehensive observations during the spring melt are still rare.

The transition from winter into spring marks a period of rapid change in the sea ice physical and biogeochemical system. During this period, both abiotic and biotic processes throughout the ice column can contribute to inorganic carbon redistribution. Throughout the dark and cold polar winter, biological activity is minimal and net heterotrophic [*Deming*, 2010; *Niemi et al.*, 2011], and sea ice permeability is significantly decreased [e.g., *Petrich and Eicken*, 2010]. These factors contribute to the buildup of CO_2 within brine

channels as salinity increases and carbonate minerals precipitate [e.g., *Miller et al.*, 2011b; *Fransson et al.*, 2013]. As a result, sea ice can become a source of CO_2 to the atmosphere with the advance of spring, when surface temperatures and sea ice permeability increase [*Nomura et al.*, 2010a; *Papakyriakou and Miller*, 2011]. Carbon dioxide fluxes across the atmosphere-ice boundary are highly variable during this period of rapid temperature change, due to strong variability in surface ice conditions (chemical and physical) and in the state of the overlying snow cover [e.g., *Delille*, 2006; *Zemmelink et al.*, 2006; *Nomura et al.*, 2010b; *Papakyriakou and Miller*, 2011; *Geilfus et al.*, 2012]. As spring warming advances further, CO_2 fluxes have been observed to switch direction, with the melting ice surface contributing to extensive CO_2 uptake from the atmosphere as an apparent result of brine dilution within the warming, melting ice [e.g., *Delille*, 2006; *Nomura et al.*, 2010a; *Geilfus et al.*, 2012]. This CO_2 drawdown over late spring-early summer is potentially enhanced by the dissolution of the calcium carbonate within the melting sea ice matrix [e.g., *Dieckmann et al.*, 2008, 2010; *Thomas et al.*, 2010; *Loose et al.*, 2011; *Rysgaard et al.*, 2011]. In the lower ice column, increased porosity associated with warming enhances the gravity-driven drainage of brines into under-ice waters, transferring salts and inorganic carbon into the surface mixed layer [*Jones and Coote*, 1981; *Rysgaard et al.*, 2007] and enhancing seawater flushing up into the ice [*Zhou et al.*, 2013]. Furthermore, biological processes within the bottom ice can drive carbonate system variability as solar radiation and temperature increase. Over this period, autotrophic communities in the bottom ice experience dense growth as nutrients are replenished from seawater under increasing light levels [e.g., *Gosselin et al.*, 1985; *Cota et al.*, 1987; *Arrigo et al.*, 2010].

Changes in the Arctic sea-ice carbonate system at this critical time of year are beginning to receive more direct attention [*Rysgaard et al.*, 2007; *Nomura et al.*, 2010a, 2010b, 2013a; *Miller et al.*, 2011b; *Geilfus et al.*, 2012; *Fischer*, 2013; *Fransson et al.*, 2013]. However, few studies have documented the evolution of the inorganic carbon system over multiple weeks bridging the transition from winter to spring at a single location [*Miller et al.*, 2011b; *Fischer*, 2013]. The goal of this study was to fill this knowledge gap by documenting and interpreting changes in inorganic carbon speciation, stable carbon isotopes, and CO_2 fluxes during the early-melt period in a landfast ice system near Resolute Passage, Nunavut. Here we present data for carbonate system parameters (total alkalinity, total inorganic carbon, and pCO_2), stable isotopes (δ^{18}O-H_2O, δ^{13}C-TIC), chlorophyll *a*, and CO_2 flux measurements over a 6 week time series to characterize the carbon cycle throughout the entire ice column, from the atmosphere-ice interface to the ice-seawater interface. Further, we test the application of stable carbon isotopes to distinguish between abiotic and biotic influence on the inorganic carbon cycle [e.g., *Papadimitriou et al.*, 2004, 2007, 2009; *Munro et al.*, 2010]. For example, as meltwater dilutes brine in warming ice, $CaCO_3$ dissolution can increase brine dissolved inorganic carbon (DIC), and enrich trapped brines in ^{13}C (i.e., increase the ^{13}C/^{12}C ratio), if the CO_2 generated during precipitation is lost from solution. In contrast, photosynthetic uptake of DIC in the bottom ice enriches brines in ^{13}C while depleting brine DIC, as algae preferentially fix ^{12}C-bearing CO_2. Several studies have utilized stable carbon isotopes to trace inorganic carbon cycling in Antarctic seasonal sea ice [e.g., *Kennedy et al.*, 2002; *Papadimitriou et al.*, 2007, 2009; *Munro et al.*, 2010], and our work represents an extension of this approach to the Arctic sea ice system.

2. Materials and Methods

2.1. Field Site Description: Resolute Passage

The 2010 *Arctic-Ice Covered Ecosystem* (Arctic-ICE) study took place in Resolute Passage, Nunavut, Canada (Figure 1a). The sea-ice camp was situated on smooth, landfast, first-year sea ice, above a water column approximately 140 m deep, in the Canadian Arctic Archipelago (CAA; Figure 1b). This region is typically characterized by a seasonal ice cover for at least 10 months of the year, with landfast ice persisting for at least half of that time [*Melling et al.*, 2008] and reaching its maximum thickness by mid-April [*Shirasawa and Ingram*, 1997]. We collected time series samples from 7 May to 19 June 2010 on a 3 day rotation schedule.

2.2. Discrete Snow, Bulk Ice, Brine, and Under-Ice Surface Water Sampling

Discrete samples of snow, sea ice, brine, and under-ice surface water were collected at a new undisturbed site each sampling day (Figure 1c). Daily sample location selection was based on snow depth distribution at each new site, and carbon system sampling was carried out at sites that exhibited an average snow depth
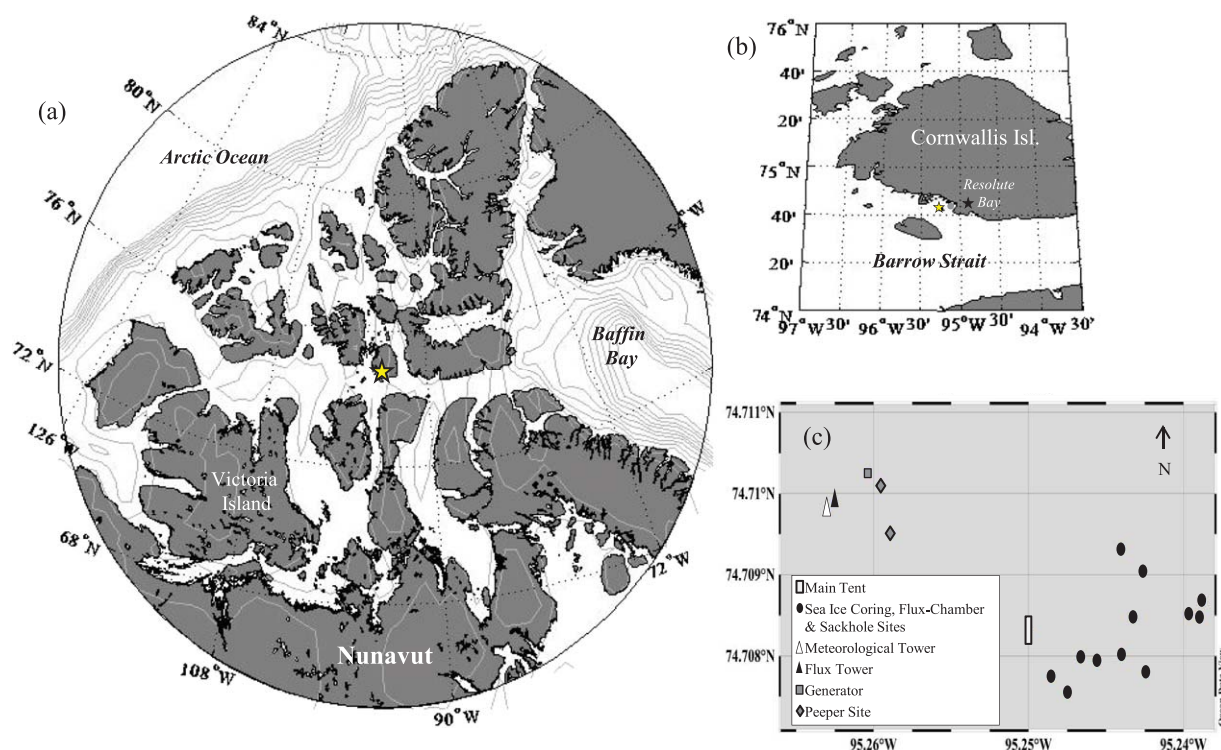
Figure 1. Map of the field study location. Clockwise from left: (a) Canadian Arctic Archipelago, yellow star indicates location of Resolute Passage ice camp site (74°42.6′N, 95°15′W); (b inset) zoom in on Cornwallis Island, study site (yellow star, as in Figure 1a) and town of Resolute Bay, NU (black star); and (c) Field camp layout.

that varied little over the course of the time series (13 ± 2 cm). Snow pits were first excavated with a flat metal shovel or spatula. Profiles of snow temperature (T) were recorded at 2 cm vertical intervals using a temperature probe (Traceable® Digital Thermometer, Model 4000, Control Company). A vertical profile of snow samples, using a 2 cm density cutter, was then collected into plastic bags (Nasco Whirl-Pak®) and melted at room temperature in the Polar Continental Shelf Project (PCSP) facility for salinity (S) determination. On several occasions, additional snow samples were collected in the same manner for oxygen isotope ratio (δ^{18}O-H_2O) measurements.

Duplicate full depth sea-ice cores were extracted using a Kovacs Mark II 9 cm diameter corer, immediately subsectioned into 20 cm (2 cm × 10 cm) lengths, and sealed into gas tight Tedlar™ film bags. The headspace was immediately removed using a hand pump, with careful attention not to apply vacuum to the sample by halting pumping as the flexible bag collapsed around the sea ice core. Bagged ice core sections were kept in coolers until transport back to the PCSP laboratory, where the ice was melted at room temperature in the dark. Once the ice had melted, Tygon tubing was fitted to the Tedlar™ bag spigot, and any excess air (released as the ice sample melted) was removed. Assuming that the air released from the melting sample is in equilibrium with the melt, we calculate that less than 1% of the total carbon is lost from the system when removing the excess air. We further expect this loss to negligibly influence the stable isotope signatures of the melt. Once the excess air was carefully removed, samples were gently mixed to homogenize the melt, and subsamples for geochemical parameters were removed through the Tygon tubing. To reduce the accidental influence of the snow cover on bulk melt parameters in the uppermost core subsections, the segments of the sea ice in direct contact with the snow layer (which we chose as the upper 10 cm, for consistency) were removed. Individual full depth sea-ice cores were also collected for T and S determination as described in *Galindo et al.* [2014].

Sackholes were drilled with a 20 cm auger to depths of 130, 90, and 60 cm within the ice adjacent to the ice core drilling location (within 2–3 m). Immediately after drilling, sackholes were sealed at the ice/snow interface with plastic-covered, high-density foam plugs to limit gas exchange. Brine was allowed to accumulate in the sackholes over the course of the coring day (~5–6 h) then collected into 10 L cubitainers (Fisher

Scientific) using an aquarium pump (QuietOne 800, Lifeguard Aquatics) to sample close to the bottom of the sackhole. Cubitainers were filled slowly to reduce bubble entrainment. Any bubbles or headspace in the cubitainer was removed by overfilling before sealing. The filled containers were then covered in black plastic bags to limit light exposure.

At the same sampling location, seawater from the ice-water interface was collected through an open core hole using the aquarium pump. As with sackhole brine samples, 10 L cubitainers were filled with seawater, compacted and capped without headspace and placed in a black plastic bag to shield them from light. Collected brine and under-ice seawater were then transported to the heated sampling tent and immediately subsampled. Each cubitainer was inverted gently several times to homogenize the contents before collecting subsamples for geochemical parameters through Tygon tubing on the cubitainer spigot.

Subsamples for total inorganic carbon (TIC) and total alkalinity (TA) were collected into 250 mL borosilicate glass reagent bottles (Pyrex), allowed to overflow 1 full volume, and stoppered after the headspace was adjusted to 1% of the sample volume. Samples were preserved with 200 μL saturated $HgCl_2$ solution before sealing and securing the stoppers with silicon-free high vacuum grease (Apiezon Type-M) and vinyl electrical tape (3M). Stable carbon isotope samples (δ^{13}C-TIC) were collected into 30 mL amber soda-lime glass bottles (Wheaton), allowed to overflow 1 bottle volume, preserved with 30 μL saturated $HgCl_2$, and sealed with no headspace using Poly-Seal-lined caps (Wheaton) secured with Parafilm-M (Sigma-Aldrich). Subsamples for δ^{18}O-H_2O determination were collected into rinsed 20 mL clear borosilicate glass vials, and sealed using polypropylene caps with fluoropolymer resin/silicone septa (VWR) after *McLaughlin et al.* [2012]. All samples were stored at room temperature in the PCSP laboratory until shipping south for analysis.

2.3. Continuous and In Situ Observations
2.3.1. In Situ Peepers and Atmospheric pCO₂
The mixing ratio of CO_2 (XCO$_2$, ppmv) within the sea ice was monitored using in situ peeper gas samplers following *Miller et al.* [2011a]. To secure the peepers in place, holes were drilled through the sea ice to the underlying water using a 5 cm auger with a power head, and allowed to fill with seawater to the freeboard line, freezing the peepers in place. Peeper arrays were deployed at two locations within 200 m of an eddy covariance CO_2 flux tower and about 100 m apart (Figure 1c). Peeper set 1 was set at depths of 10, 50, 70, and 90 cm (total ice thickness =142 cm) and Peeper set 2 at depths of 60, 100, 145, and 152 cm below the top of the ice (total ice thickness = 145 cm, so the 152 cm peeper was in the underlying water). After allowing the peepers to freeze in and equilibrate with the surrounding ice (3–5 days), each array was sampled at 72 h intervals by circulating the air within the system in a closed loop through a Continuous Automated CO_2 Sampler (CACS) system equipped with a LI-820 NDIR gas analyzer (Li-COR Environmental; flow rate = 1 mL min^{-1}). The maximum peak height determined by the detector was used to generate sample XCO$_2$. The CACS system was calibrated on-site against CO_2 gas standards (1968 ppm and 958 ppm; PRAX-AIR) at the start and end of the sampling program. Local atmospheric XCO$_2$ was recorded ∼1.5 m off the snow surface using the CACS during each sampling event. The XCO$_2$ (ppmv) values were converted to pCO_2 (μatm) using internal cell pressure and the average saturation vapor pressure of water [*Weiss and Price*, 1980], determined for in situ brine *T* and *S* conditions during our study.

2.3.2. Sea Ice Temperature Structure
Sea ice and snow *T* were continuously monitored using a thermocouple array secured within a 2 m long PVC tube and frozen into the ice next to the meteorological tower (Figure 1c). Ice column *T* measurements were taken every 3 s by a data logger (Campbell Scientific Model CR3000) and recorded in 1 min averages over 23 depths from +0.21 m above the ice surface (upper 21 cm of snow) to −2.20 m below the ice surface (through the 140 cm thick ice column and into the upper surface waters).

2.3.3. Flux Chambers
Fluxes of CO_2 across the surface of the ice were measured using a LI-8100 automated soil CO_2 flux system (LiCOR Biosciences). To create an enclosed headspace for chamber measurements, a PVC collar (10 or 5 cm high) was pressed into the snow cover or cut into the ice surface using a custom-made metal toothed collar. The flux chamber was then placed on the collar, and snow was packed around the ensemble to ensure a tight seal. Once the flux chamber was in place, the domed lid was closed and ambient CO_2 within the enclosed chamber was measured over time. The net change in pCO_2 over a 10–15 min interval was used to calculate the flux. At each sampling location, chamber CO_2 flux was measured at the snow surface (on

Table 1. Pooled Standard Deviation, SDp[a], of Duplicate Analyses for Geochemical Parameters

Parameter	Units	Under-Ice Surface Water		Bulk Ice		Sackhole Brine	
		SDp	k	SDp	k	SDp	k
S (probe)		0.2[b]	40	c		c	
TIC	μmol kg^{-1}	4.4	10	0.26	3	18	25
TA	μmol kg^{-1}	3.7	9	4.8	32	4.6	23
δ^{13}C-TIC	‰ VPDB	0.14[d]	51	e		0.10	44
δ^{18}O-H$_2$O	‰ VSMOW	0.03	3	0.03	4	f	

[a]IUPAC [1997], where k is the number of measurement pairs.
[b]Maximum error on corrected probe salinity was observed to be ± 0.2; 92% of corrected values fell within ± 0.1.
[c]Salinity in bulk ice and sackhole brine samples was measured in single samples only, so SDp could not be determined.
[d]SDp for water δ^{13}C-TIC samples taken from a larger pooled data set including the 11 under-ice surface water samples from this study.
[e]Limitations on sample volume meant there were no true duplicate bulk ice δ^{13}C-TIC samples, we expect a similar analytical precision as for seawater and brine.
[f]Measurements of δ^{18}O-H$_2$O are not reported for brine.

snow) and the ice surface (immediately under the snow) at three sites within a 1 m $\times$ 1 m area of uniform snow character. Several CO$_2$ flux measurements were also carried out over hoar frost (with snow above the crystalline hoar frost layer removed), slush (mix of snow and snow melt), and melt ponds (completely melted snow) as the season advanced.

2.4. Geochemical Analyses

The salinity (S) of under-ice surface seawater, snow melt, bulk ice, and brine samples was measured with a hand-held conductivity meter (WTW Cond 330i) calibrated to a 0.01 mol L^{-1} KCl standard solution. Brine samples with S values greater than the instrument measurement range ($S = 0$–70) were diluted with equal parts of distilled water before measurement. Reported accuracy for the hand-held conductivity meter is ± 0.1 over a salinity range of 0–42. For under-ice seawater samples, hand-held probe measurements were corrected by comparing S measured in seawater samples (collected from a 1 m $\times$ 1 m covered hole in a heated tent, using a Niskin bottle) with the hand-held conductivity meter and those measured by a CTD deployed through the same hole (SBE 19plusV2 CTD, Sea-Bird Electronics; $N = 40$). Here S is reported on the Practical Salinity Scale 1978 (PSS78) without units

Total inorganic carbon (TIC) was measured coulometrically following *Dickson et al.* [2007] using either a VINDTA 3D (Marianda) or SOMMA system at the Institute of Ocean Sciences, Sidney, B.C., Canada. Following TIC analysis, total alkalinity (TA) was determined using an open-cell titration with an automated Dosimat 665 titrator (Metrohm) and Red Rod pH combination electrode (Radiometer Analytical). The titration endpoints were determined by nonlinear least squares fit [*Dickson et al.*, 2007]. Both TIC and TA were calibrated against certified reference materials (CRM 88 and 101) provided by Andrew Dickson (Scripps Institute of Oceanography).

The δ^{13}C-TIC samples were analyzed at the GEOTOP Stable Isotope Laboratory (Université du Québec à Montréal) using a Micromass Isoprime continuous flow isotope ratio mass spectrometer equipped with a MultiFlow (Isoprime) automated injection system. Carbon isotopic values are reported in per mil (‰) with respect to Vienna PeeDee Belemnite (VPDB) referenced to the NBS-19 and LSVEC scale (standard error ± 0.1‰). The δ^{18}O-H$_2$O samples were analyzed at COAS Stable Isotope Laboratory (Oregon State University) using a Thermo Finnigan DeltaPlus XL isotope ratio mass spectrometer. Oxygen isotopic values are reported in ‰ with respect to Vienna Standard Mean Ocean Water (VSMOW) (standard error ± 0.05‰).

Analytical precision for each geochemical parameter measured in this study is listed in Table 1, where SDp refers to the pooled standard deviation [*IUPAC*, 1997] of k pairs of measurements.

3. Calculations

3.1. Bulk Ice Brine Salinity, Sackhole Brine Temperature, and Brine Volume

The salinity of brine contained in the original bulk ice samples, S_b, was approximated from the phase relationship between brine salinity and in situ temperature, as described in *Petrich and Eicken* [2010] for brine

$T > -23°C$. This same phase relationship was rearranged and applied to approximate in situ brine temperature, T_{Sb}, of collected sackhole brine samples from measured salinity [*Petrich and Eicken*, 2010]. We determine brine volume fraction (V_b/V) as a function of sea ice temperature and salinity after *Cox and Weeks* [1983], as summarized in *Petrich and Eicken* [2010], using the temperature-dependent empirical functions described by *Cox and Weeks* [1983] and *Leppäranta and Manninen* [1988]. As bulk ice density was not measured in our samples, we assume the absence of air (i.e., $V_a/V = 0$) for simplicity in our calculations.

3.2. Partial Pressure of CO_2 in Sackhole Brine, Bulk Ice, and Under-Ice Surface Seawater

Partial pressure of CO_2 (pCO_2) in sackhole brine and under-ice surface seawater samples was calculated from measured TIC, TA, S (or S_b), and T (or T_{Sb}) using CO2Sys [*Pierrot et al.*, 2006]. Following *Delille et al.* [2007], we used carbonic acid dissociation constants, K_1 and K_2, determined by *Mehrbach et al.* [1973], refit by *Dickson and Millero* [1987], and dissociation constants for $KHSO_4$ determined by *Dickson* [1990]. Brine pCO_2 values determined from bulk ice samples were calculated from measured bulk ice TA and TIC corrected to brine salinity (S_b). Here we have assumed that the seawater derived carbonic acid dissociation constants of *Mehrbach et al.* [1973] are valid at low temperature and high salinity. Recent work has shown, however, that the extrapolation of these constants to S and T values beyond those of seawater could introduce errors of up to 45% ($\bar{x} = 17\%$) in the calculation of pCO_2 from DIC and TA at in situ brine T and S conditions [*Brown et al.*, 2014].

3.3. Modeling the Effects of Freshwater Dilution and Warming on Brine pCO_2

To model the impacts of freshwater dilution and warming on brine pCO_2 over the melt season, we chose a representative early season peeper measurement ($pCO_2 = 1207$ μatm, $T = -4.45°C$, depth = 60 cm, 19 May) and corresponding sackhole brine sample from a similar depth interval and ice temperature ($S = 82$, $T = -4.83°C$, depth = 60 cm, 17 May). We calculated S_b of the peeper sample using measured T (section 3.1) and corrected the sackhole brine S_b and TA to this value. Even though sackhole brine samples undoubtedly lost some CO_2 to the atmosphere during collection and handling (section 2.2), sackhole brine TA will not be affected by off-gassing and should therefore be representative of brine TA within the ice column. A brine TIC value was then calculated using peeper pCO_2 and sackhole brine TA using CO2sys (see section 3.2). A model for freshwater dilution was then determined by diluting S, TA, and TIC conservatively to the new S_b value associated with T.

The end member selection in our model is nontrivial, however, and the slope of the derived freshwater dilution line is extremely sensitive to this value. Great care was taken to derive a starting value most representative of observations from the early sampling period to model the evolution of pCO_2 with warming. Choosing an early season end-member start value based on bulk ice TIC and TA measurements would have biased the model as solid $CaCO_3$ contained in the ice sample would dissolve during melt and contribute to artificially reducing calculated pCO_2 compared to in situ conditions. Similarly, the use of the corresponding brine TIC value would have underestimated the pCO_2 change with dilution if CO_2 loss had occurred during sample collection. Calculated brine pCO_2 values are both sensitive to physical conditions (T, S) and directly dependent on inorganic carbon concentrations in solution, meaning that the early season peeper pCO_2 value, on its own, without directly associated TIC and TA values, could not be used to model the brine chemistry responses. Therefore it was determined that this combination of sackhole brine measured TA and in situ peeper pCO_2 produced an initial end-member start value that most closely represented early season observations and could then be used to model the impact of freshwater dilution with warming.

4. Results

4.1. Snow Cover Characteristics

Across our sampling sites, average snow depth varied little over the course of the time series (13 ± 2 cm). The snow exhibited relatively isothermal depth profiles, with average temperatures (T) that followed air T fluctuations (Figure 2a), progressing from coldest values ($-7.5°C$) on 10 May toward a fully melting ($T \approx -0.5°C$) snow cover by 10 June (snow melt onset 6 June) [*Mundy et al.*, 2014]. Snow salinity (S) (Figure 2b) diminished with distance from the ice surface, with the highest S at the snow base (up to 12.3 at the start of the sampling on 10 May) decreasing toward $S = 0$ in the upper snow. Snow $\delta^{18}O$-H_2O became more
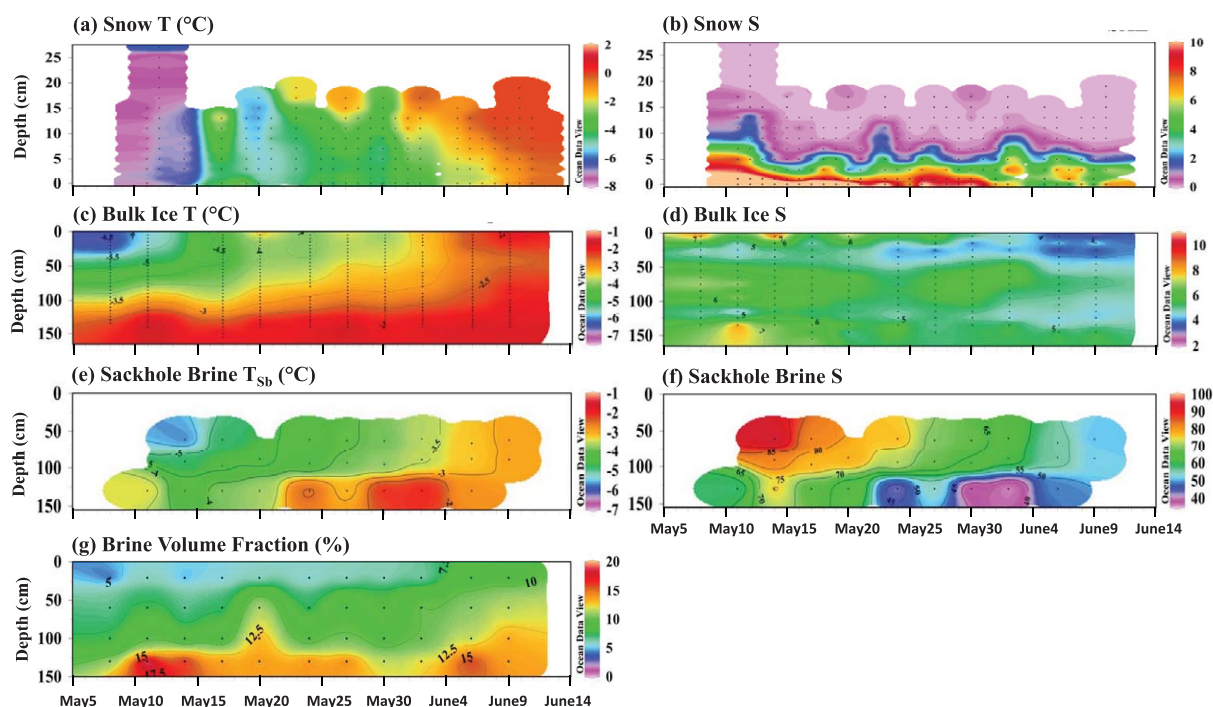
Figure 2. Six week time series of physical conditions in the snow and sea ice. (a) Snow temperature; (b) snow salinity; (c) bulk ice temperature; (d) bulk ice salinity; (e) sackhole brine temperature; (f) sackhole brine salinity; and (g) brine volume fraction. Note the differences in color scales for different sample types.

isotopically depleted away from the saline snow base, with values of $-11.01 \pm 0.03‰$ ($N = 2$) at the snow base and $-20.72 \pm 1.17‰$ ($N = 4$) in the upper snow ($S = 0$).

Snow base S started to decrease more rapidly between 31 May and 2 June (Figure 2b), as the upper snow cover T rose above $-2°C$ (Figure 2a). Ice lenses were found in the upper 5–9 cm of the snow from 8 June onward, signifying surface snow melt percolation and refreezing. Melt ponds began to form on 14 June [*Mundy et al.*, 2014].

4.2. Landfast Sea Ice
4.2.1. Physical Properties
Sea ice thickness (142 ± 2 cm) and freeboard (10 ± 1 cm) remained relatively constant at our sampling site over the duration of this study. Temperatures in bulk ice and brine (Figures 2c and 2e) increased as surface air T increased from an average of $-12°C$ in early May to around $0°C$ in early June [*Else et al.*, 2014]. Sea ice T exhibited a minimum of around $-7°C$ at the ice surface at the beginning of the program, corresponding to high bulk ice S of 6.3–9.6 (Figures 2c and 2d). Bulk ice S was generally lower underneath the surface (10–30 cm), and became progressively less saline with time (Figure 2d). Likewise, S in the bottom 20 cm of ice generally decreased over the course of the sampling period (Figure 2d). Brine volume fraction (V_b/V, %) had a similar distribution to that of sea ice T, with lowest values found in the cold upper ice (3%) increasing with depth toward the warmer bottom ice (11%) at the start of the sampling program (Figure 2g). High brine volume fraction (9–14.8%) was observed throughout the ice column as it approached an isothermal T distribution at the end of the sampling period.

The bulk ice $\delta^{18}O$-H_2O data illustrate a weak gradient in the lower two-thirds of the ice column (50–140 cm) that changed only subtly over the sampling period (Figure 3). In these layers, bulk ice $\delta^{18}O$-H_2O was enriched with respect to the under-ice surface water ($-1.83 \pm 0.06‰$) and upper ice (10–30 cm; $-0.47 \pm 0.06‰$). Bottom ice $\delta^{18}O$-H_2O appeared to increase over the first half of the sampling program and remained at $+0.07 \pm 0.03‰$ after 20 May.

Sackhole brine S decreased dramatically over the time series, at all depths sampled (Table 2). Calculated brine T tracked the patterns in bulk ice, but with lower absolute values (cf. Figure 2c and 2e). The correspondence between brine T and bulk ice T suggests that the sackhole samples successfully integrated the
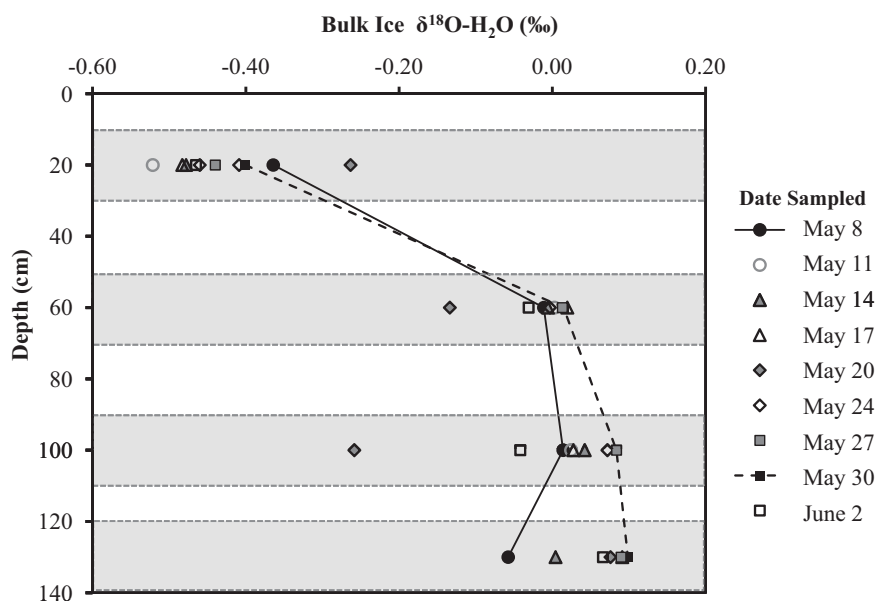
Figure 3. Bulk ice melt stable oxygen isotope δ^{18}O-H$_2$O signatures plotted by depth in the ice column and distinguished by sampling date. Gray shading indicates depth interval of sea ice sample (20 cm).

physical and chemical constituents of the ice column above the sackhole depths. Sackhole brine S decreased as the bulk ice warmed (depicted as change with sampling day in Table 2), and as increased permeability in the ice column permitted in situ melt, brine drainage, and mixing with under-ice surface water.

4.2.2. Sea Ice CO$_2$ System

Both TIC and TA exhibited strong positive correlations with S in bulk ice (10–110 cm; $r^2 = 0.93$ and $r^2 = 0.97$, respectively) and sackhole brine ($r^2 = 0.96$ and $r^2 = 0.97$, respectively) samples. To account for the conservative dilution of TIC and TA as a function of S, bulk ice and sackhole brine TIC and TA have been normalized to the average S of under-ice surface seawater ($S = 32.5$) using the convention, sTIC = TIC/S × 32.5. Observations of salinity-normalized TIC (sTIC), TA (sTA), and stable carbon isotopes (δ^{13}C-TIC) are shown in Figure 4.

At the beginning of the sampling program, bulk ice sTIC throughout the majority of the ice column (10–110 cm; 2224.5 ± 53.7 μmol kg^{-1}) was higher than under-ice surface seawater values (2132.1 ± 5.0 μmol kg^{-1}). Bulk ice sTIC in the lower ice (from 90 cm to the bottom) decreased significantly over the time series, and bottom ice sTIC was always lower than water column values, decreasing to an average value of ≈ 1220 μmol kg^{-1} by the end of the sampling period. As with sTIC, bulk ice sTA was much higher than water column values (sTA = 2333.9 ± 51.7 μmol kg^{-1} versus 2226.9 ± 3.7 μmol kg^{-1} for seawater) through the majority of the ice column (10–110 cm), but was consistently lower in the upper ice layer after 10 May (10–30 cm; Figure 4b). In the bottom ice layer, sTA was closer to water column values throughout the sampling period (bottom ice = 2278 ± 113 μmol kg^{-1}). Salinity-normalized TA did not significantly change over the

Table 2. Trends in Sackhole Brine Geochemical Parameters Over the Sampling Period[a]

	Brine	S^b (/day)	sTIC (μmol kg^{-1}/d)	sTA (μmol kg^{-1}/d)	δ^{13}C-TIC (‰/d)	δ^{13}C-TIC (‰/S)	δ^{13}C-TIC (‰/sTIC)	δ^{13}C-TIC (‰/sTA)
60 cm	Slope	−1.90	14.01	16.23	0.03	−0.02	0.001	0.002
	r^2	0.72	0.26	0.31	0.86	0.76	0.21	0.38
90 cm	Slope	−1.16	5.43	7.88	0.04	−0.03	0.003	0.004
	r^2	0.99	0.62	0.85	0.84	0.81	0.30	0.56
130 cm	Slope	−1.14	−3.28	−1.57	0.02	0.01	−0.005	−0.002
	r^2	0.56	0.22	0.06	0.09	0.09	0.40	0.05

[a]In columns 3–6, regression slopes represent the change in each measured parameter per day at each sampling depth. The final three table columns (7, 8, and 9) present the change in brine stable isotope composition per change in brine S, in sTIC and in sTA. Coefficients of determination (r^2) are shown for each regression.
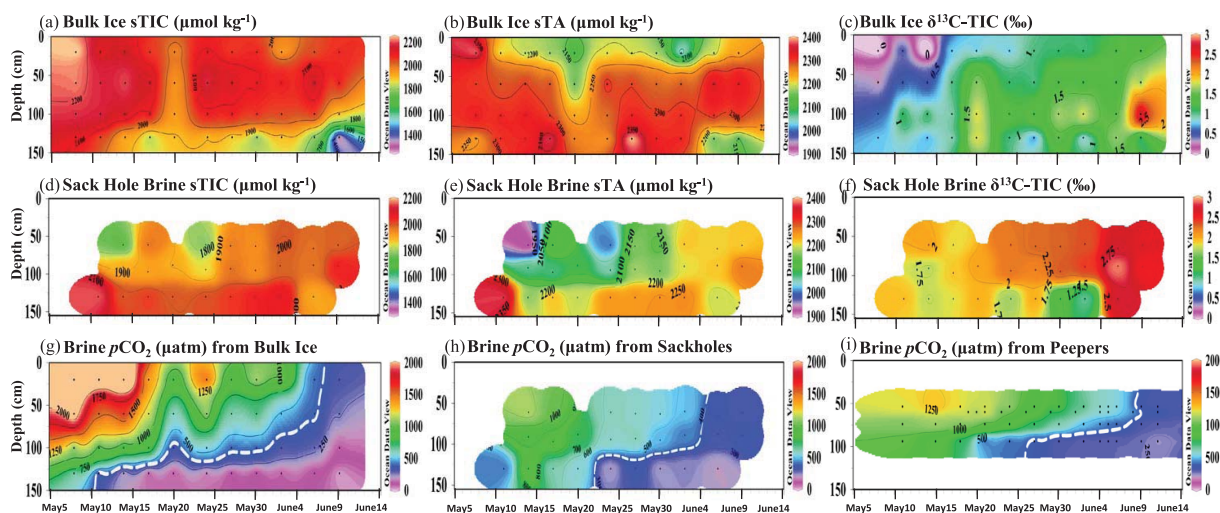[b]Brine S is reported on the Practical Salinity Scale 1978 (PSS78) without units.

Figure 4. Six week time series of carbonate system parameters in sea ice and sackhole brine samples. Prefix "s" denotes TA and TIC data were normalized to a salinity of 32.5, the average S of under-ice surface seawater. (a) Bulk ice sTIC; (b) bulk ice sTA; (c) bulk ice δ^{13}C-TIC; (d) sackhole brine sTIC; (e) sackhole brine sTA; (f) sackhole brine δ^{13}C-TIC; (g) brine pCO$_2$ as calculated from bulk ice TA and TIC; (h) brine pCO$_2$ as calculated from sackhole brine TA and TIC; (i) brine pCO$_2$ as measured from in situ peepers. White dashed lines in Figures 4g-4i illustrate saturation with respect to atmospheric pCO$_2 \approx 380$ μatm. For reference, average under-ice surface seawater values: TIC = 2227 ± 4 μmol kg^{-1}, TA = 2132 ± 5 μmol kg^{-1}, δ^{13}C-TIC = $+0.69 \pm 0.08‰$, and pCO$_2$ = 383 ± 7 μatm.

course of our sampling season at any depth (Figure 4b and Table 3). Sackhole brine sTIC and sTA values from the upper to middle parts of the ice (60 and 90 cm) were always lower than the under-ice surface seawater average (Figures 4d and 4e). In general, the salinity-normalized values in sackhole brines increased over the sampling period in both the upper and middle parts of the ice (60 and 90 cm) but decreased in the deepest sackholes that extended to the bottom of the ice (Table 2).

The TA/TIC ratio measured within the bulk ice increased throughout the ice column over the time series (Figure 5a). Early in the sampling season, bulk ice TA/TIC was similar to the underlying surface seawater (1.045 ± 0.001), then increased as the season progressed following the sTIC decrease and brine volume increase (Figures 2g and 4a, respectively). Sackhole brine TA/TIC was higher than bulk ice and surface seawater values in the early season, and increased marginally over the sampling period (Figure 5b). The discrepancy between bulk ice and sackhole brine TA/TIC values likely reflects brine channel connectivity in the highly permeable ice column (Figure 2g), as well as the contribution of CaCO$_3$ dissolution, mobilizing excess alkalinity out of the solid phase into the brines (see section 5).

4.2.3. Stable Carbon Isotope Ratios

Bulk ice δ^{13}C-TIC values were quite variable (-0.52 to $+3.38‰$) and generally became more enriched with time as the ice pack warmed (Figure 4c and Table 3). Unlike TIC and TA, bulk ice δ^{13}C-TIC values showed no relationship with S ($r^2 = 0.03$). Isotopic values throughout the majority of the ice column (10–110 cm) became enriched in ^{13}C over the course of the 6 week time series, whereas bottom ice samples followed no such trend (Table 3). We observed a strong negative relationship between δ^{13}C-TIC and sTIC within the 90–110 cm section of the ice column (slope = -0.007, $r^2 = 0.71$; Table 3), but not at any other depths. The δ^{13}C-TIC values in bottom ice samples showed no correlation with any of the other variables sampled.

Sackhole brine δ^{13}C-TIC values ranged from $+0.97$ to $+2.96‰$ (Figure 4f). Brine values were generally isotopically heavier than those measured in bulk ice and always isotopically heavier than the under-ice surface seawater ($+0.69 \pm 0.08‰$). In contrast to bulk ice samples, sackhole brine in the middle-ice horizon (60 cm and 90 cm depth) became more isotopically enriched over the course of the sampling program, as S decreased with increasing ice T (Table 2). Isotopic enrichment within the 60 and 90 cm sackholes was more strongly correlated with S and sTA than with sTIC (Table 2). Brine isotopic values in the deepest sackhole samples (130 cm) were only weakly correlated with other measured parameters (Table 2).

4.2.4. Brine pCO$_2$

Brine pCO$_2$ diminished considerably with depth in the ice column and with time. This was observed in values calculated from bulk ice (3326–2 μatm; Figure 4g) and sackhole brine (1128–200 μatm; Figure 4h)

Table 3. Trends in Bulk Ice Geochemical Parameters Over the Sampling Period[a]

Bulk Ice		T (°C/d)	S[b] (/day)	Brine Vol. ([Vb/V]/d)	sTIC (μmol kg^{-1}/d)	sTA (μmol kg^{-1}/d)	δ^{13}C-TIC (‰/d)	δ^{13}C-TIC (‰/sTIC)
10–30 cm	Slope	0.119	−0.04	0.0012	−4.60	−2.65	0.04	−0.003
	r^2	0.93	0.33	0.59	0.18	0.07	0.55	0.24
50–70 cm	Slope	0.075	−0.02	0.0014	−2.06	1.75	0.03	−0.004
	r^2	0.95	0.05	0.55	0.08	0.11	0.43	0.35
90–110 cm	Slope	0.043	−0.02	0.0012	−6.42	−0.03	0.06	−0.007
	r^2	0.79	0.08	0.33	0.48	0.00	0.54	0.71
Bottom 20 cm	Slope	0.010	−0.05	−0.0008	−15.65	−4.38	0.01	−0.001
	r^2	0.16	0.43	0.08	0.39	0.14	0.00	0.09

[a]In columns 3–8, regression slopes represent the change in each measured parameter per day within each ice horizon. The final table column (9) presents the change in bulk ice stable isotope composition per change in sTIC. Coefficients of determination (r^2) are shown for each regression.
[b]Bulk Ice S is reported on the Practical Salinity Scale 1978 (PSS78) without units.

measurements, and for in situ peeper measurements (1280–230 μatm; Figure 4i). Under-ice surface water pCO$_2$ values (383 ± 7 μatm) were close to equilibrium with respect to the atmosphere (384 ± 4 μatm) for the duration of the sampling program and showed little temporal change. Brine pCO$_2$ in the upper ice (10–30 cm) remained above saturation with respect to the atmosphere until 6 June (Figure 6a), whereas bottom ice was undersaturated with respect to the under-ice surface seawater after 11 May (Figure 4g). Brine pCO$_2$ calculated from bulk ice and sackhole brine samples (Figures 4g and 4h) and measured in situ with the peepers (Figure 4i) was closely related to brine volume (a function of T and S; Figure 7).

4.3. Ice-Atmosphere CO$_2$ Flux

In general, fluxes from all surfaces were small and ranged from +0.058 to −0.051 μmol m^{-2} s^{-1} (Figures 6b and 6c; negative fluxes imply CO$_2$ uptake into the ice). We observed a general transition from positive fluxes from the ice (into the atmosphere) during the first 8 days of observations toward a negative flux (into the ice) after 2 June. Fluxes from the snow were generally positive (toward the atmosphere) or neutral (Flux$_{CO2}$ = 0) during the whole sampling period, while the highest negative fluxes occurred over slush and melt ponds, or directly into the ice. The transition from positive to negative fluxes shown in Figures 6b and 6c corresponds with gradual warming of the snow and ice surfaces, with an apparent threshold T of the ice surface between −3.5 and −2.7°C (Figure 2c). A hoar frost layer measurement in the middle of the time series showed zero net flux (Figure 6c), while late-season measurements in the slush and melt-ponds
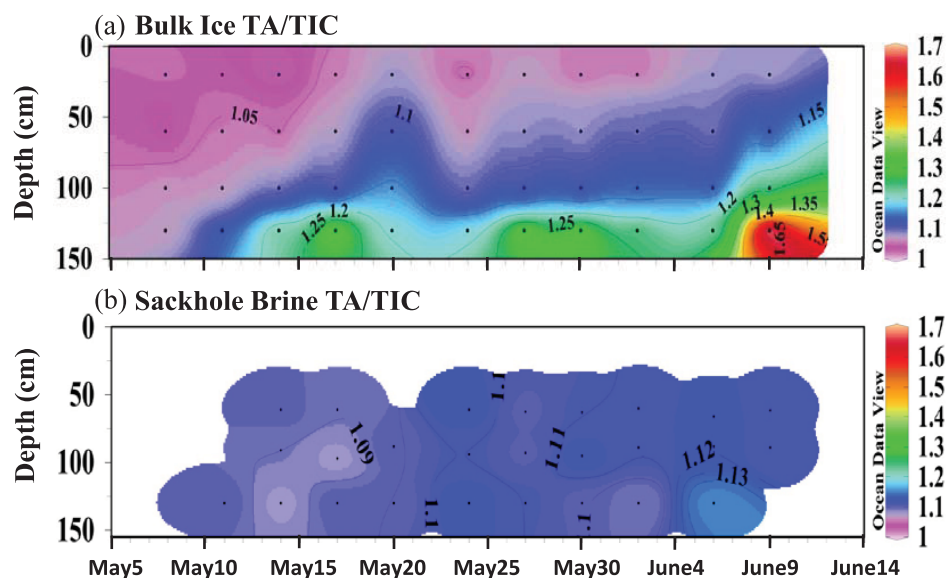

Figure 5. Six week time series of TA/TIC (a) within bulk ice and (b) sackhole brine samples. For reference, measured TA/TIC of the underlying surface seawater was 1.045 ± 0.001.
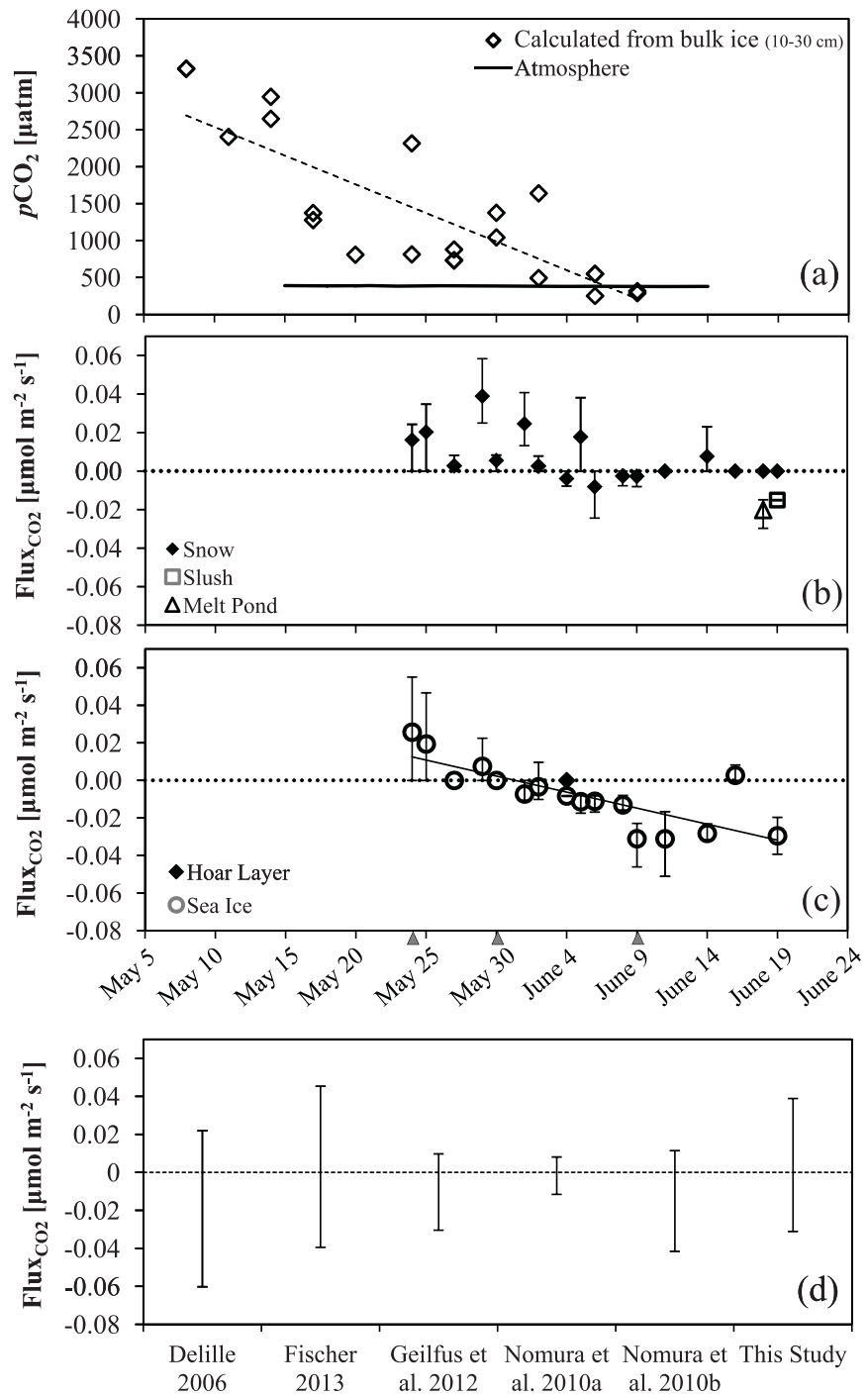
Figure 6. (a) Time series of upper ice brine pCO_2 calculated from bulk ice melt TIC and TA (10–30 cm). The dashed line in Figure 6a represents the linear trend through the data points. Atmospheric pCO_2 was $\approx$ 380 ppm over the study period, indicated by the solid black line. (b) Time series of CO_2 flux measurements on snow (black-filled diamonds), slush (open square), and melt pond (open triangle) surfaces. The vertical bars on each data point represent the data range (maximum and minimum measurements from each day). (c) Time series of CO_2 flux measurements over sea ice (open circles) and hoar frost (filled diamond) surfaces. The solid black line illustrates the linear trend through the average sea ice data points. Positive fluxes are from the interface toward the atmosphere. Gray triangles on x-axis represent the time points chosen for calculations in Table 4; the vertical bars on each data point in Figures 6b and 6c represent the data range (maximum and minimum measurements from each day). (d) Spring season CO_2 flux chamber measurements reported in other Arctic and Antarctic sea ice studies. Vertical lines denote the range of values measured.
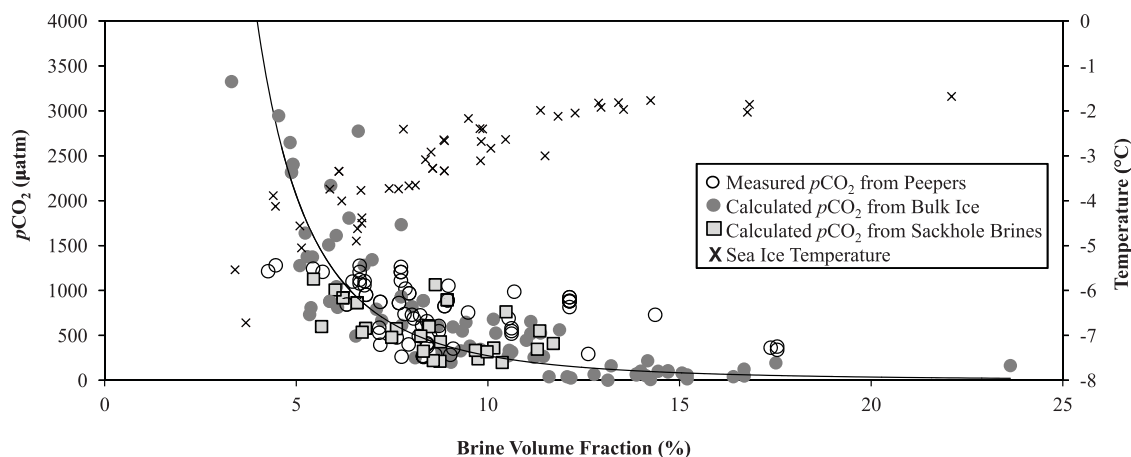
Figure 7. Sea ice temperature (black x's) and brine pCO_2 (circles and squares) plotted against calculated brine volume fraction. Open circles represent measurements from in situ peepers, gray circles and squares represent values calculated from TA and TIC measurements in bulk ice and sackhole brines, respectively. Brine pCO_2 values (calculated from bulk ice) can be related to brine volume fraction by an exponential curve, $pCO_2 = 221765\ (V_b/V, \%)^{-2.9}$ ($r^2 = 0.65$; black line).

showed negative (downward) CO_2 fluxes (Figure 6b). Over this period, pCO_2 within the upper ice column (10–30 cm) was up to an order of magnitude higher than atmospheric pCO_2, and remained higher than atmospheric values until at least 3–5 June (Figure 6a).

5. Discussion

5.1. Methodological Considerations in the Determination of pCO_2 Within Spring Sea Ice

One novel aspect of this study was the use of various observational methods to describe the sea ice inorganic carbon system and its evolution over the early melt period. Combining measurements of discrete inorganic carbon system parameters, from ice melt and brine, with continuous pCO_2 measurements in the ice column, provides a means to intercompare and evaluate alternative approaches to the same questions and assess possible disequilibrium in the sea ice carbonate system during this dynamic time of year.

All three methods used to determine brine pCO_2 in this study are associated with their own uncertainties, adding caveats to any direct comparison. For instance, sackhole samples are composed of brine collected over an unknown volume of sea ice. At best, they represent an averaged value for the ice column, and at worst a value heavily biased toward the most permeable (warmest) layers of the ice, with a major influence from underlying seawater. The calculation of brine pCO_2 from measured TIC and TA under the high salinity, low temperature conditions of natural sea ice is also problematic. The application of seawater derived carbonic acid dissociation constants outside of their empirical ranges has been shown to generate calculated pCO_2 values to within no better than 10% of measurements, with potential bias of as much as 150% [*Brown et al.*, 2014]. Relative to sackhole samples, material from discrete sea ice cores can be tied with more certainty to a specific region of the ice column, and bulk sea ice melt has salinity values closer to the empirical range of carbonic acid dissociation constants. However, the analytical error associated with the measurement of TIC and TA in melt samples, combined with potential sample handling artefacts (e.g., CO_2 loss with air space before melts are subsampled, see section 2.2), are compounded when TIC and TA values are scaled to brine S, which can be as much as 6–25 times that of measured bulk melt. In addition, $CaCO_3$ dissolution during ice melt will add TA and TIC to solution in a 2:1 ratio, underestimating calculated pCO_2 at brine salinity. Direct measurement of brine pCO_2 with the in situ peepers alleviates many of these issues; however, the process of installing the peepers by rapidly freezing them into an intact ice column also adds uncertainty as to whether the pCO_2 values are truly representative of the undisturbed ice cover and compounds the impacts of local heterogeneity between peepers and coring sites.

In spite of these caveats, all three observational methods illustrated a significant decrease in pCO_2 within the sea ice over the course of the sampling program (Figures 4g–4i). In addition, pCO_2 observations agreed
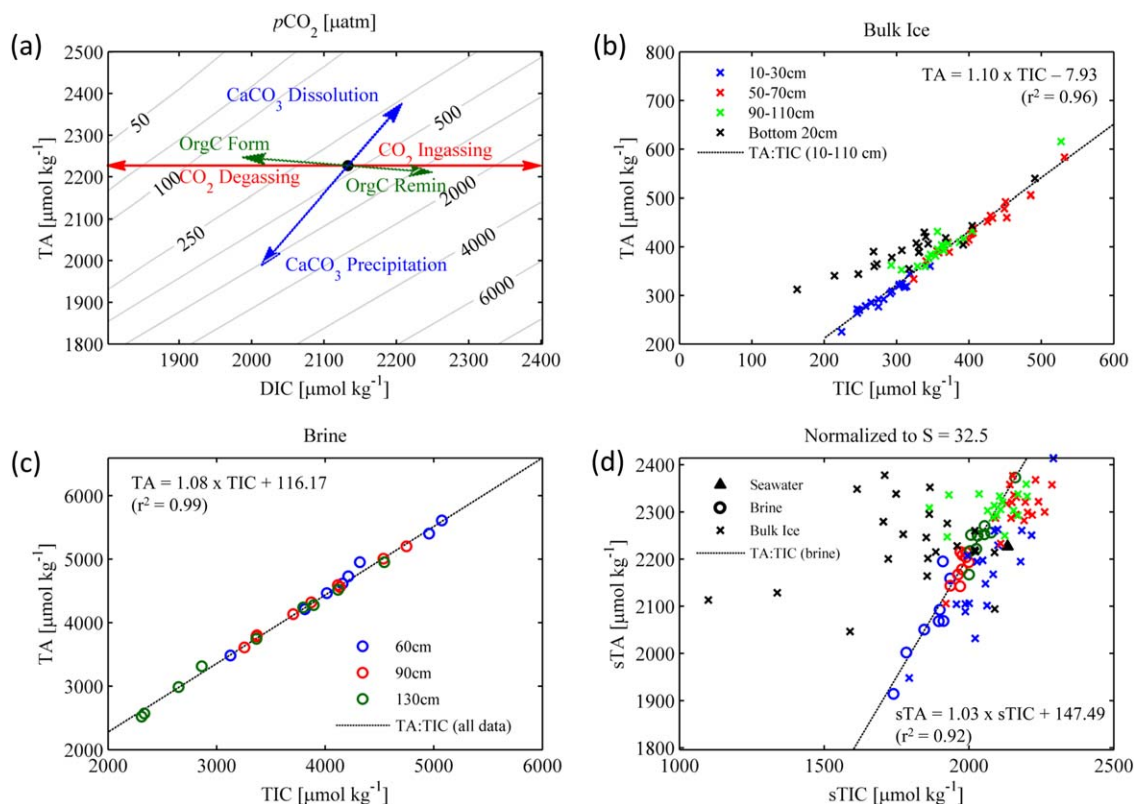
Figure 8. (a) Impact of different biological (green arrows) and geochemical (blue and red arrows) processes on the concentration of DIC and TA in a typical seawater sample (black-filled circle), and their associated impact on seawater pCO_2 (gray contour lines). (b) Measured TA and TIC in bulk ice, with a regression line fit to the upper and middle-ice column samples (10–110 cm). (c) Sackhole brine measured TA and TIC, with a regression line fit through all data points. (d) Salinity normalized ($S = 32.5$) TA (sTA) plotted against salinity normalized TIC (sTIC) for sackhole brine samples (circles, and linear regression line), bulk ice (x's), and average under-ice surface seawater (black-filled triangle). Color coding in Figure 8d follows that in Figure 8b for bulk ice and Figure 8c for brine.

reasonably well between all three methods when plotted with respect to sea ice physical parameters (e.g., brine volume fraction; Figure 7). These comparisons suggest that despite the methodological uncertainties discussed above, brine pCO_2 determined either by in situ measurement or calculated from inorganic carbon system parameters can be used to shed light on different processes controlling the inorganic carbon system in sea ice over the study period.

5.2. Controls on the Sea Ice Inorganic Carbon System Over the Spring Warming Period

Our observations over the early-melt period illustrate an influence of sea ice on the seasonal air-sea CO_2 exchange during this dynamic season. High brine pCO_2 at the beginning of the sampling program in early spring appeared to be associated with a relatively small CO_2 efflux from the ice (Figure 6c). As warming progressed, the gradual decrease in brine pCO_2 culminated with CO_2 uptake into the melting ice when brine was undersaturated with respect to the atmosphere (Figures 4g–4i and 6c). This decrease in pCO_2 throughout the sea ice column could have been associated with processes that influence TA, TIC, and pCO_2 in the brine (Figure 8a), including: biological production, CO_2 degassing, brine dilution, and calcium carbonate ($CaCO_3$) dissolution. Based on our observations of TIC and TA, the vertical sea ice column can be divided into distinct biogeochemical "zones": namely (1) the bottom ice (120–140 cm) and ice-water interface, (2) the middle-ice column (50–110 cm), and (3) the ice-atmosphere interface and upper ice (10–30 cm). Our data indicate differences in the dominant processes influencing the carbonate system in these different zones over the time series.

In spite of the observed biogeochemical zonation over the early-melt period, high brine volume fractions (>5%; Figure 2g) indicate that brine convection should have connected, at least partially, all three zones and the underlying water column during our study [e.g., *Carnat et al.*, 2013; *Zhou et al.*, 2013]. Brine convection over the full ice column promotes solute (e.g., nutrients, DIC) exchange between the sea ice brine
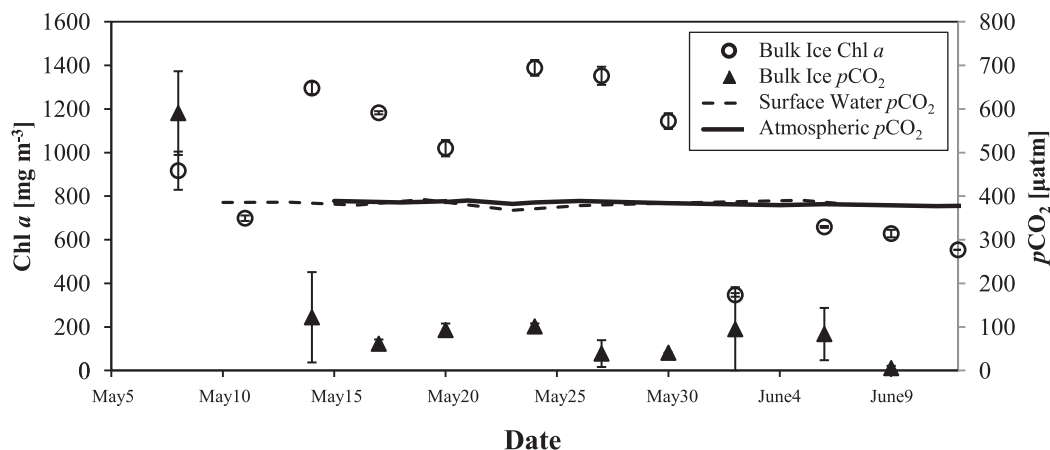
Figure 9. Time series of chlorophyll *a* concentrations in the bottom 3 cm of sea ice and pCO_2 in the bottom 20 cm of sea ice. Bottom ice pCO_2 was calculated from measured values of bulk ice TA and TIC. The black solid line indicates measured atmospheric pCO_2 and the black dashed line illustrates pCO_2 values determined from seawater TIC and TA samples collected at the ice-water interface. Chlorophyll *a* data from medium snow depths sites are derived from *Galindo et al.* [2014].

system and the surface ocean. However, these exchanges are limited when brines become density stratified due to ice melt [*Zhou et al.*, 2013]. *Zhou et al.* [2013] describe a "transition" stage during the early-melt period when the ice column approaches an isothermal temperature distribution with brine volume fractions >5%. During this transition stage, the brine density profile is expected to be unstable, contributing to convection throughout the ice column [*Zhou et al.*, 2013]. This is followed by a "warm" stage with isothermal sea ice temperatures and a stable brine density profile, promoting brine stratification and limiting exchanges within the ice column and with the underlying seawater. Based on the profile of sea ice *T* (Figure 2c) and brine *S* (Figure 2f), our observational period appears to include both the "transition" and "warm" melt stages described by *Zhou et al.* [2013]. In our discussion below, we thus consider the impact of brine convection (and concomitant seawater mixing) on the biogeochemical parameters and pCO_2 measured in each "zone" of the sea ice column over the study period.

5.2.1. Bottom Ice and Ice-Water Interface
The bottom ice (120–140 cm) and the ice-water interface make up the lowermost biogeochemical zone in the sea ice column. Samples collected from the bottom 20 cm of the sea ice were characterized by low pCO_2 values that were undersaturated with respect to the atmosphere and the seawater after 10 May (Figure 4g), as well as TA and TIC values that deviated from the remaining ice column (Figure 8b). These data suggest that $CaCO_3$ dissolution and/or organic matter formation may have influenced pCO_2 in this layer (Figure 8a).

Neither CO_2 degassing nor mixing with seawater could have accounted for these low bottom ice pCO_2 values. Since these values were lower than those of the underlying seawater, gas exchange and mixing would have resulted in a pCO_2 increase in the bottom ice. Likewise, high sea ice permeability and seawater flushing are thought to remove solid $CaCO_3$ salts from this layer [*Rysgaard et al.*, 2007], suggesting CO_2 drawdown by $CaCO_3$ dissolution would be limited. Rather, high biological productivity in the bottom ice cores is the more likely explanation for the low observed pCO_2. Indeed, >95% of algal biomass was concentrated within the bottommost 3 cm of the ice cover during our study period [*Galindo et al.*, 2014], and the low pCO_2 in the bottom 20 cm of the ice corresponded well with low sTIC and high chlorophyll *a* until 2 June (Figure 9), when bottom ice algae appeared to slough off into the water column [*Mundy et al.*, 2014]. Even though surface water pCO_2 was generally in equilibrium with atmospheric values, localized productivity in the bottom ice led to a dramatic pCO_2 decrease as chlorophyll *a* increased at the beginning of our study (Figure 9). This evidence suggests the bottom ice algal community significantly drew down TIC within the bottom ice and thus played a dominant role in driving bottom ice pCO_2 distributions, as observed in previous studies [e.g., *Gleitz et al.*, 1995; *Delille et al.*, 2007; *Munro et al.*, 2010; *Geilfus et al.*, 2012; *Papadimitriou et al.*, 2012].

5.2.2. Middle-Ice Column (50–110 cm)
The middle-ice column (50–110 cm) makes up the next biogeochemical zone. Here dilution of TA and TIC was more or less conservative as sea ice *T* increased and *S* decreased (Figures 8b and 8c). Linear regression
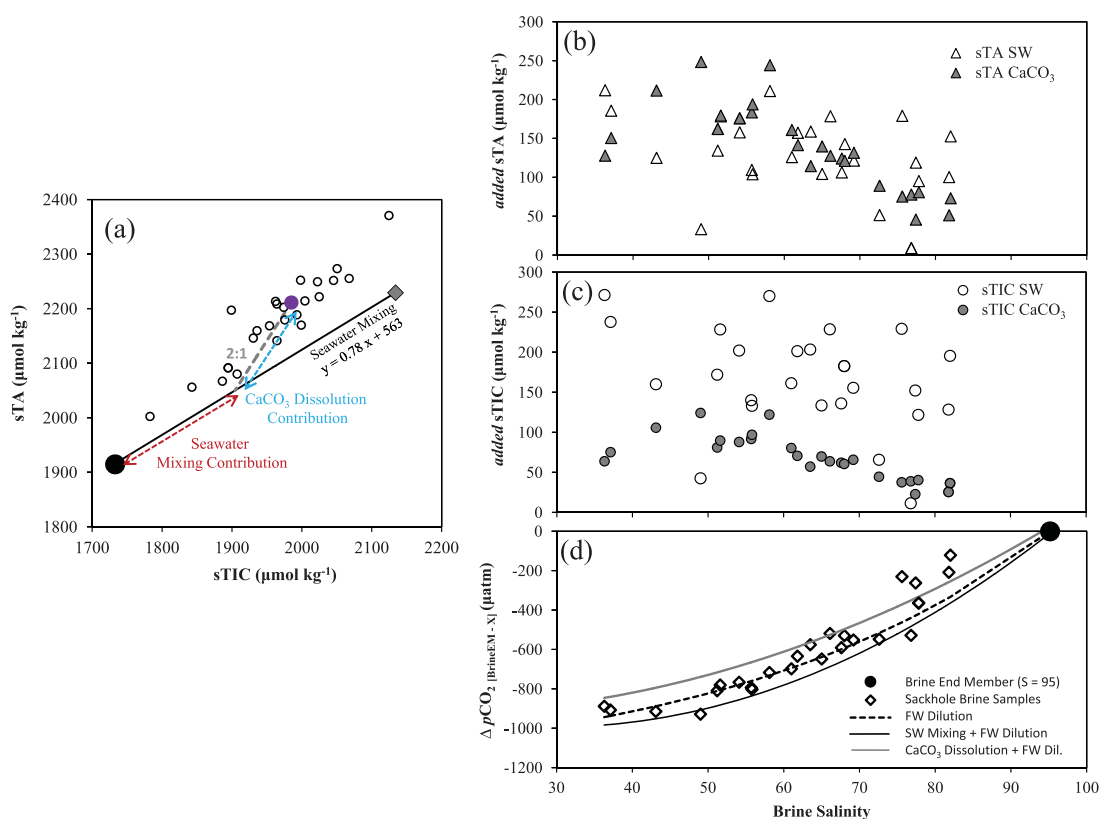
Figure 10. Contributions of seawater mixing and $CaCO_3$ dissolution to sackhole brine sTA, sTIC, and pCO_2 changes over the time series. Prefix "s" denotes TA and TIC values are normalized to the average under-ice surface seawater salinity of 32.5. (a) Sackhole brine sTA verses sTIC (open circles, Figure 8d) compared to the mixing line (black line; slope = 0.78) between the most saline brine value end member (black-filled circle) and seawater (gray-filled diamond), and the 2:1 TA:TIC addition from $CaCO_3$ dissolution (gray dashed line). The contribution of seawater mixing (red dashed arrow) and $CaCO_3$ dissolution (blue dashed arrow) to one particular sample (purple-filled circle) is illustrated. (b) sTA added by either seawater mixing (open triangles) or $CaCO_3$ dissolution (gray-filled triangles) as a function of brine salinity for each sample; (c) as in Figure 10b, but for sTIC. (d) The calculated difference ($\Delta pCO_{2[Brine\ End\ Member\ -\ X]}$) between pCO_2 in the sackhole brine end member ($S = 95$; black-filled circle) and that calculated from freshwater dilution (black dashed line), seawater mixing and freshwater dilution (black solid line), or $CaCO_3$ dissolution and freshwater dilution (gray solid line), plotted as a function of brine salinity.

lines drawn through brine and bulk sea ice data points approach the origin (intercepts of -7.9 ± 10.7 μmol kg^{-1} and 116.2 ± 61.0 μmol kg^{-1} for bulk ice and sackhole brine, respectively, Figures 8b and 8c), indicating the dominant influence of freshwater dilution (in situ melt) over the time series.

5.2.2.1. Controls on Brine sTA and sTIC
Normalizing TA and TIC to constant salinity removes the freshwater dilution influence, but the derived sackhole brine sTIC and sTA values still follow a quasi-linear trend (circles, Figure 8d). This remaining covariation in the salinity-normalized sackhole brine values indicates that additional processes contributed to a change in both sTA and sTIC over the time series.

Dissolution of $CaCO_3$ and seawater mixing should contribute sTA and sTIC to brine in a predictable manner. Dissolution of $CaCO_3$ would add TA:TIC to the brine in a 2:1 ratio (equation (1)), whereas mixing with under-ice surface seawater ($S = 32.5$) would dilute brine along a mixing line with a slope of 0.78 (using a brine end member defined by the $S = 95$ sample; Figure 10a).

$$CaCO_3 + CO_2 + H_2O + Ca^{2+} + 2HCO_3^- \tag{1}$$
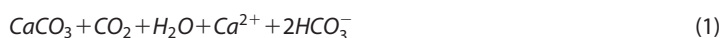
The slope of the brine sTA versus sTIC relationship in Figure 8d (dashed line) is 1.03, only slightly lower than the under-ice surface seawater sTA:sTIC ratio of 1.045; this suggests a combination of $CaCO_3$ dissolution and seawater mixing may have contributed to increasing brine sTA and sTIC, even as ice melt diluted TA and TIC more-or-less conservatively. *Geilfus et al.* [2012] likewise observed a strong correlation between brine sTA and sDIC ($r^2 > 0.999$), but with a slope much lower than the underlying seawater TA:DIC ratio (0.89 versus 1.049). They attributed this deviation in slope to a combination of $CaCO_3$ precipitation and CO_2 degassing

removing both TA and DIC from the brine solution. An sTA:sDIC slope of 1:1 would indicate that CO_2 was lost from (or taken up by) the brine in proportion to $CaCO_3$ precipitated (or dissolved). *Geilfus et al.*'s [2012] observations of a slope < 1 suggest that additional CO_2 had degassed from the ice, beyond that associated with $CaCO_3$ formation. The brine sTA:sTIC slope between 1 and 2 we observed suggests that the brine chemistry at our study site was influenced by both $CaCO_3$ dissolution (equation (1)) and mixing with under-ice surface seawater.

To clarify the following discussion, we use the term "seawater mixing" to generalize the exchange of brine with seawater as brine drainage proceeds. That is, as sea ice warms, brine draining from more permeable ice results in a return-flow of seawater into the ice, contributing to export of brine into the underlying seawater, and localized brine dilution within the ice matrix [*Vancoppenolle et al.*, 2010; *Zhou et al.*, 2013]. If seawater mixing were solely responsible for the quasi-linear trend of sackhole brine samples in Figure 8d, we would expect brine sTIC and sTA to approach seawater values along a mixing line between two end members: early-season saline brine and seawater. We can use the most saline sackhole brine sample ($S = 95$, 14 May, 60 cm) and average seawater ($S = 32.5$) as end members to define such a mixing line (Figure 10a, slope = 0.78). In contrast, $CaCO_3$ dissolution would produce a 2:1 slope in the sTIC versus sTA relationship, according to equation (1) (Figure 8a). The combination of these two processes in variable proportions, however, would produce a slope between 0.781 and 2, as observed in our data set (Figure 8d). Our data can thus be best explained by a combination of $CaCO_3$ dissolution and seawater mixing as primary controls on sTA and sTIC in the middle-ice column.

To consider the variable impact of seawater mixing (SM) and $CaCO_3$ dissolution (CD) on sTIC and sTA measured in each brine sample, we first determine the equation of a line with a 2:1 slope that connects each data point with the seawater mixing line (Figure 10a) using equation (2):

$$m_{SM}x + b_{SM} = m_{CD}x + b_{CD} \qquad (2)$$

where the subscript SM refers to the slope and intercept for the seawater mixing line (0.78 and 563, respectively), and subscript CD refers to the slope and intercept of the 2:1 line for $CaCO_3$ dissolution. For the latter, the slope is 2 and the intercept is dictated by the sample. The distance from the brine end member value (black-filled circle) to the intersection of the seawater mixing line with a 2:1 line from each sample point represents the seawater mixing contribution to sTA and sTIC in that sample (red arrow, Figure 10a). The difference between the 2:1 line intersection point on the seawater line for each sample and the measured sample value represents the increase in sTA and sTIC due to $CaCO_3$ dissolution (blue arrow, Figure 10a). These calculations indicate that seawater mixing and $CaCO_3$ dissolution added roughly equal amounts of sTA to sackhole brines as salinity was diluted over time (Figure 10b). In contrast, seawater mixing contributed more sTIC than $CaCO_3$ dissolution (Figure 10c). The sTA and sTIC contributions associated with $CaCO_3$ dissolution became quantitatively more important with the dilution of brine salinity.

Our analyses suggest that $CaCO_3$ dissolution within melting sea ice could have contributed as much as 250 μmol kg^{-1} TA to spring brines at our study site (Figure 10b). To put this value in context with other studies, *Rysgaard et al.* [2013] found average concentrations of 100–900 μmol kg^{-1} of $CaCO_3$ (as ikaite) in winter sea ice in Greenland, with $CaCO_3$ concentrations highest in the upper ice column. Their study illustrated that $CaCO_3$ in the upper ice accounted for the majority of bulk ice TA, whereas this proportion decreased toward the ice-water interface where more TA was found in solution. In contrast, an early spring study by *Nomura et al.* [2013a] found $CaCO_3$ precipitates in only ≈30% of their sea ice, snow, and slush samples, accounting for between 27 and 54 μmol L^{-1} of the inorganic carbon in the bulk melt. As the dissolution of 1 μmol kg^{-1} $CaCO_3$ would contribute 2 μmol kg^{-1} of TA to solution, our calculated ΔTA from $CaCO_3$ dissolution falls between these two studies (Figure 10b). These differences could simply reflect regional heterogeneity, or they may illustrate the speed at which precipitate dissolution occurs in the transition from winter into early spring.

5.2.2.2. Controls on Middle-Ice pCO$_2$

Even though seawater mixing and $CaCO_3$ dissolution were found to contribute a similar amount of sTA to brine solutions (Figure 10b), the difference in the TA:TIC ratio of inorganic carbon contributed by these two processes will result in a differential impact on sackhole brine pCO$_2$. By adding the ΔsTA and ΔsTIC values determined in Figures 10b and 10c to TA and TIC predicted from freshwater dilution of brine alone, we can estimate the change in sackhole brine pCO$_2$ associated with these two processes. Figure 10d illustrates the change in pCO$_2$ from the initial sackhole brine end member ($S = 95$) associated with: (i) freshwater dilution

alone (black dashed line), (ii) seawater mixing and freshwater dilution (black solid line), or (iii) $CaCO_3$ dissolution and freshwater dilution (gray solid line). Comparison of the observed sackhole pCO_2 values with these different prediction lines indicates that sackhole brine pCO_2 can be almost entirely attributed to freshwater dilution alone, as seawater mixing and $CaCO_3$ dissolution effectively cancel each other out at $S < 75$ (Figure 10d). From this analysis we conclude that the influences of seawater mixing and $CaCO_3$ dissolution on sackhole brine sTA and sTIC are negated when their impact on pCO_2 is considered, and as such, freshwater dilution can be modeled as the primary factor controlling pCO_2 in our sackhole brine samples, at least at low salinities.

Sackhole brine pCO_2, calculated from measured TA and DIC, was generally lower than that measured in the peepers and calculated from the bulk ice measurements over the time series (Figures 4g–4i). This discrepancy suggests that sackhole observations may not adequately represent pCO_2 within the majority of the sea-ice column. Although sackhole brine collection methods and sample handling practices attempted to limit exposure of samples to the atmosphere, off-gassing of such high pCO_2 brines as they were being collected could potentially explain some of the discrepancy between peeper and sackhole measurements (Figures 4h and 4i).

Holding T constant, a decrease in brine S by freshwater dilution will increase CO_2 solubility by reducing the concentration of ions in solution and by shifting the carbonate equilibrium toward bicarbonate [HCO_3^-] and carbonate [CO_3^{2-}] ions, thus reducing pCO_2 [*Zeebe and Wolf-Gladrow*, 2001]. This process alone should explain the drop in our calculated and measured pCO_2 values as sea-ice temperature increased over the course of the sampling season (Figures 4g–4i). The in situ peeper pCO_2 observations were well correlated with T, which controls CO_2 solubility and ice permeability [*Petrich and Eicken*, 2010, Figure 11]. Below the seawater freezing point ($\approx -1.8°C$), CO_2 solubility in brine decreases as T drops and S increases. This occurs because the segregation of dissolved salts and gases during ice formation overrides the solubility increase with decreasing T, facilitating rapid CO_2 supersaturation within sea-ice brine [*Papadimitriou et al.*, 2004]. *Delille* [2006] observed a similar inverse correlation between brine pCO_2 and T in spring Antarctic sea ice, suggesting that large decreases in brine pCO_2 in spring are driven by dilution of brine as ice melts.

We calculated the theoretical brine pCO_2 that would result from direct dilution of brine inorganic carbon with warming/freshening in a closed system following section 3.3 (red diamond, Figure 11). The results of this analysis suggest that freshwater melt dilution of brine alone can explain a large portion (but not all, see below) of the drop in brine pCO_2 over the melt season. A similar analysis of dilution effects on brine pCO_2 was carried out by *Geilfus et al.* [2012] who examined the relationship between equilibrator measured pCO_2 and T within sackhole brine. However, instead of choosing an early season end-member value, these authors based their freshwater dilution curve on the average brine sTA and sTIC taken from all samples with $S < 80$. *Geilfus et al.* [2012] observed much greater variability in measured brine pCO_2 values (e.g., from 750 to 1800 μatm at $\approx -10°C$; their Figure 9), likely due to direct pCO_2 measurement within sackholes after brine had accumulated. This large spread in brine pCO_2 even at low ice T complicates the determination of the start value for the freshwater dilution line, making the choice of an average brine value most appropriate. In our study, choosing an average brine value would have heavily biased the dilution model toward later season samples and toward processes such as seawater mixing that become much more important as ice permeability increases with warming (note: this is also likely an issue for *Geilfus et al.* [2012] as 36% of their brine samples are at $T >$ freezing point, suggesting a direct influence of seawater). Bearing this in mind, we feel that the start value for our freshwater dilution model is the most appropriate characterization of observations from this study. However, we openly acknowledge that this model is highly sensitive to this start value, and that the conclusions drawn from it may change if different start values were used.

Mixing the brine end member (red diamond, Figure 11) with seawater serves to increase pCO_2 above the expected freshwater dilution line (Figures 10d and 11). This is strong evidence to indicate that seawater mixing is not a main process contributing to the pCO_2 drop within the middle-ice horizon (50–100 cm). Seawater dilution may, however, act to increase pCO_2 in the warmest, most permeable parts of the ice ($T > -2.5°C$; Figure 11) during the late melt period. In contrast, $CaCO_3$ dissolution can be invoked on its own to explain the entire depression of pCO_2 values below the freshwater dilution line in Figure 11 ($T < -2.5°C$). For example, the 273 μatm pCO_2 offset between the freshwater dilution line and peeper measurements at the same temperature (green squares, Figure 11) can be accounted for by an addition of 522 μmol kg^{-1} TA (and 251 μmol kg^{-1} TIC) to brine solution by the in situ dissolution of $CaCO_3$. These
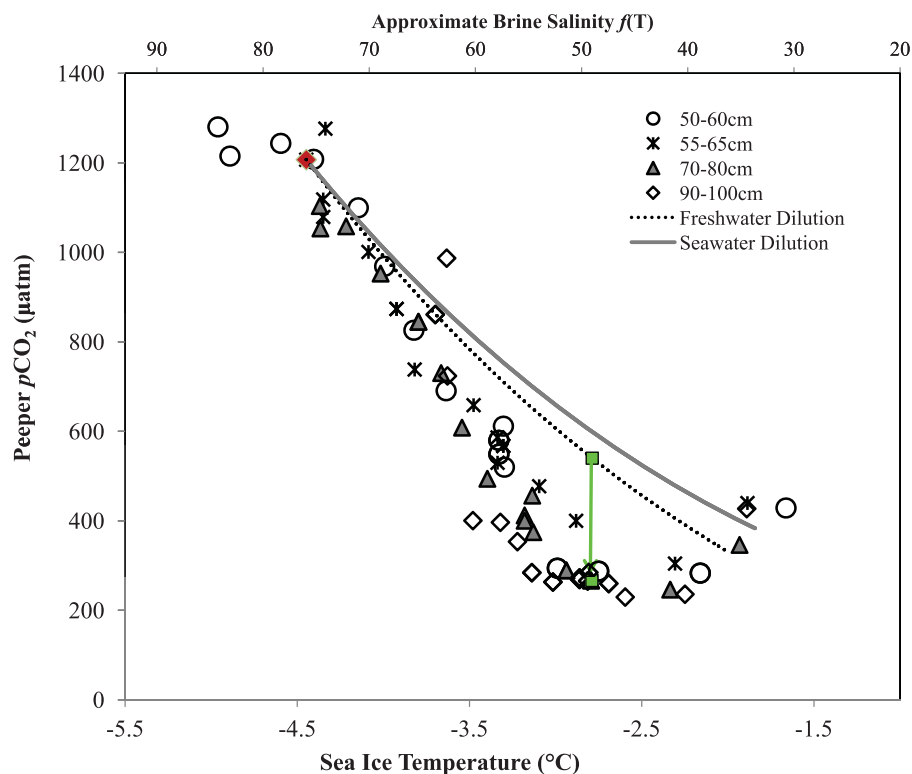
Figure 11. Sea ice pCO_2 measured with in situ peeper samplers plotted versus in situ sea ice temperature recorded from various depth intervals using a thermocouple string at our meteorological station. Brine salinity, calculated from temperature, is listed as an alternate x axis. The pCO_2 change associated with freshwater dilution alone (ice melt) is depicted by the black dashed line, starting from a hypothetical early season end member denoted by a red diamond (see text for details). The expected pCO_2 change associated with seawater dilution is depicted by the solid gray line. Peeper observations that deviate from the expected freshwater-dilution trajectory can be explained by dissolution of $CaCO_3$ depressing brine pCO_2 (green arrow; see text for details).

observations suggest that $CaCO_3$ dissolution exerts a measureable influence on brine pCO_2 within the middle-ice column, and that this influence increases with warming (or with dilution; Figure 11) until seawater mixing diminishes the signal. A similar relationship was observed within sackhole brine samples, where an increase in the contribution of sTIC from $CaCO_3$ dissolution was associated with decreasing brine salinity (Figure 10c). These observations indicate that a combination of freshwater brine dilution and $CaCO_3$ redissolution can largely explain the T-dependent changes in pCO_2 observed in the middle-ice column.

In situ pCO_2 measurements from the peepers appear to imply different conclusions about the dominant controls of pCO_2 within the middle-ice column than observations from sackhole brines. The former indicates freshwater brine dilution and $CaCO_3$ redissolution are responsible for the observed change in pCO_2 over the time series, whereas the latter needs only freshwater dilution to explain this change. Moreover, sackhole brine samples suggest the maximum $CaCO_3$ dissolution TA contribution is on the order of 250 μmol kg^{-1} (Figure 10b), less than half that determined from in situ peeper measurements (522 μmol kg^{-1} TA). Despite the limitations associated with each method of pCO_2 determination (section 5.1), we explain these seemingly contradictory results by considering the sackhole collection method bias. Seawater mixing with brine in the sackhole will dilute the original brine $CaCO_3$ precipitation signal, and as we have calculated, counteract the associated pCO_2 change. This leaves the sackhole brine sample with a greater freshwater dilution effect (as $CaCO_3$ precipitation and seawater dilution counteract each other's influence on pCO_2), even though $CaCO_3$ dissolution may have been important within the brine channels themselves, as suggested by the peeper observations. Likewise, the discrepancy in $CaCO_3$ dissolution TA contribution can be explained if the brine end member value used in Figure 10 (black-filled circle) was itself influenced by $CaCO_3$ dissolution and seawater mixing (i.e., not a true "end member"). If this were the case, the seawater mixing line slope would steepen, and result in an increased TA contribution from $CaCO_3$ dissolution (with the importance of seawater mixing reducing by an equivalent amount), reducing the gap between sackhole and peeper $CaCO_3$ dissolution estimates.
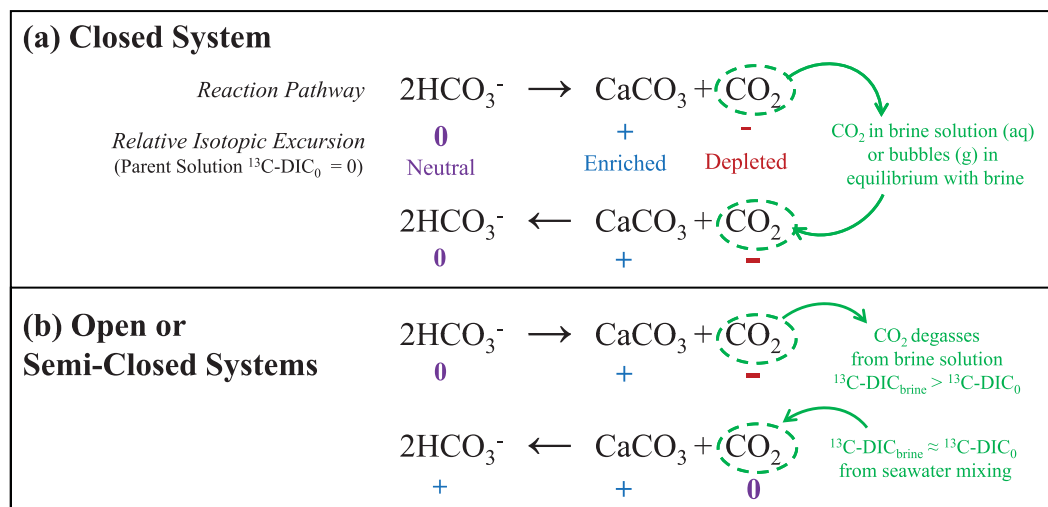
Figure 12. Relative isotopic excursions with respect to parent solution δ^{13}C-DIC during the formation and dissolution of $CaCO_3$ following equation (1), in (a) a closed system (reaction products remain in solution), or (b) open or semiclosed systems (reaction products are fully or partially removed). The relative isotopic excursion of measured HCO_3^- (DIC) in solution is illustrated as neutral (0, no change), positive ($+$, isotopically enriched, i.e., increased ^{13}C), or negative ($-$, isotopically depleted, i.e., decreased ^{13}C) relative to the parent solution δ^{13}C-HCO_3^-. Note: HCO_3^- accounts for >90% of DIC at seawater pH, so we consider it the dominant contributor to δ^{13}C-DIC in this illustration.

5.2.2.3. Impacts of $CaCO_3$ Dissolution and Seawater Mixing on δ^{13}C-TIC

Stable isotope data from bulk ice and sackhole brine samples in the interior ice column corroborate the conclusions reached above. Here we consider that bulk ice δ^{13}C-TIC reflects TIC within trapped brine and any carbonate salts or air bubbles within the ice, whereas sackhole brine δ^{13}C-TIC measurements should reflect dissolved inorganic carbon in the brine only.

Brine samples from 60 to 90 cm showed ^{13}C enrichment over the course of the sampling program (Figure 4f), as sTA and sTIC increased (Figures 4d and 4e), and as salinity decreased with increasing ice temperature. This observation is consistent with $CaCO_3$ dissolution, which could enrich brine solution through redissolution of isotopically heavy $CaCO_3$ (depending on the isotopic signature of DIC in solution). In contrast, bulk ice melt samples showed a weak signature of ^{13}C enrichment over the sampling period (10–110 cm, Figure 4c and Table 3), as sTIC decreased throughout the ice column (Figure 4a and Table 3). Unlike sackhole brines, the increase in bulk ice δ^{13}C cannot be due to higher carbonate dissolution, since all carbonate present in the sample dissolves during the melting of ice for bulk ice measurements. One possible explanation of the sTIC loss from and smaller δ^{13}C increase in bulk ice is the drainage of isotopically light brine (compared to $CaCO_3$ redissolved into the melt sample) from the porous middle-ice column near the end of the sampling period. Degassing of isotopically light CO_2 would also show a similar trend, but this mechanism was not supported by our flux data (see Figure 6c and section 5.2.3 below). Alternatively, if seawater mixing extended throughout the ice column over this period, isotopically heavy TIC could be transported upward in the ice column as a result of mixing with the biologically influenced lower layers. This could contribute isotopically heavy TIC to the middle-ice zone, while simultaneously decreasing sTIC in the bulk ice, overall. However, this mechanism would be expected to also decrease brine sTIC, which is contrary to our observations.

In a closed system, isotope effects associated with CO_2 degassing and $CaCO_3$ precipitation are negated once the backward reaction takes place upon redissolution (equation (1); Figure 12a). If the products of precipitation are separated after formation, as may be the case in open or semiclosed natural systems, the backward reaction of $CaCO_3$ dissolution can lead to brine solutions with isotopically heavy TIC if the source of CO_2 (i.e., DIC in solution) is isotopically heavier than the CO_2 lost during degassing (Figure 12b). The coupled increase in brine sTIC and isotopic ^{13}C-enrichment with warming and dilution (Figures 4d and 4f) precludes a major influence from biological assemblages in the middle-ice horizon but can be explained by the observation of seawater mixing (Figure 10) which would supply DIC with a similar isotopic signature to the parent brine solution (Figure 12b). The positive correlation between isotopic enrichment and the

Table 4. Estimate of the Equilibration Time Between Brine pCO_2 in the Upper Ice (10–30 cm) and the Atmosphere Given the Measured Flux at the Ice Surface

Date	T (°C)	S	Atmo pCO_2 (μatm)	Brine pCO_2 (μatm)[a]	Average V_b/V	Brine Volume[b] (L)	ΔCO_2 (Ice-Air)[c] (μmol)	Measured CO_2 Flux (Ice-Air)[d] (μmol m^{-2} s^{-1})	Hours to Equilibrate pCO_2[e]
24 May	−4.1	70.8	385.4	1571	0.055	16.4	882	0.026	9.5
30 May	−3.9	67	384.2	1215.3	0.057	17.0	630	0.000	
9 June	−2.2	38.6	380	303.5	0.089	26.8	−91	−0.031	0.8

[a]Brine pCO_2 calculated from bulk ice melt TIC and TA.
[b]Calculated brine volume in 0.3 m vertical $\times$ 1m $\times$ 1m horizontal plane.
[c]Number of moles of CO_2 lost/gained by brine volume upon equilibration with the atmosphere (i.e., brine pCO_2 = atmospheric pCO_2).
[d]Measured flux from the ice to the atmosphere.
[e]Hours to reach equilibration between brine pCO_2 and atmospheric pCO_2 over the 0.3 m thickness of the ice.

increase in sTIC and sTA with warming (Table 2) implies $CaCO_3$ dissolution into brine solution was an important contributor to the brine isotopic signature, as previously observed by *Papadimitriou et al.* [2004], as seawater mixing alone would have had negligible impact on brine δ^{13}C-TIC.

5.2.3. Upper Ice

The upper ice (10–30 cm) and ice-atmosphere interface make up the final biogeochemical zone. Bulk ice sTA was persistently lower in this layer than the rest of the ice column (Figure 4b). Stable oxygen isotope values in this layer also distinguish it from the ice column below (Figure 3; upper ice is isotopically light), and suggest either faster sea ice growth rates (isotopic fractionation between seawater and forming ice is reduced at higher sea ice growth rates [e.g., *Toyota et al.*, 2013]) or the influence of snow meltwater penetration [*Nomura et al.*, 2010a].

As with the middle-ice horizon (50–110 cm), freshwater dilution was the most important process controlling TIC and TA concentrations in the upper ice (10–30 cm; Figure 8b). Brine pCO_2 in the upper ice was significantly higher than atmospheric values until at least 2 June (Figure 6a). Over this same period, we measured a small CO_2 efflux from both the snow and ice surfaces (Figures 6b and 6c). In contrast, we observed CO_2 uptake into the snow-free ice later in the season, at a time when we measured no flux across the snow surface itself. This implies that processes in the snow impeded the transport and exchange of CO_2. High brine volume fractions (almost always >5%; Figure 2g), higher ice temperatures (>−5°C after 16 May; Figure 2c), and high sackhole brine volume recovery (holes filled quickly with high salinity liquid) indicate that the sea ice was highly permeable throughout our study. This further suggests that the sea ice should have been a source of CO_2 to the atmosphere over this entire period, as brine pCO_2 was persistently oversaturated with respect to the atmosphere (Figures 4g–4i).

In a highly permeable ice column, the pCO_2 difference between sea ice brine and the overlying air has been cited as the main driver of air-sea ice CO_2 flux [*Delille*, 2006; *Nomura et al.*, 2006; *Geilfus et al.*, 2012]. We measured a small positive CO_2 flux from the sea ice toward the atmosphere at the beginning of our time series (Figure 6c), which can be explained by the strong pCO_2 gradient between brine in the upper 30 cm of ice and the atmosphere (Table 4). Other spring studies have observed positive CO_2 fluxes of a similar magnitude using flux chamber measurements in the early melt season (Figure 6d). These were likewise accompanied by strong pCO_2 gradients between brine and the atmosphere [*Delille*, 2006; *Nomura et al.*, 2010a, 2010b; *Geilfus et al.*, 2012; *Fischer* 2013], and suggest CO_2 loss from brine to the atmosphere begins once the sea ice is sufficiently permeable [e.g., *Delille*, 2006; *Geilfus et al.*, 2012].

Using calculated brine volume, the ideal gas law, and the brine-atmosphere pCO_2 gradient (Table 4), we can calculate the number of moles of CO_2 that would need to be lost from brine in the upper ice (0.3 m^3) to reach equilibrium with the atmosphere. On 24 May, for example, 0.9 mmol of CO_2 would be lost to the atmosphere if the pCO_2 gradient between brine in the upper ice and the atmosphere were diminished to zero (i.e., brine pCO_2 = atmospheric pCO_2). The CO_2 flux measured between the ice and the atmosphere on 24 May (0.026 μmol m^{-2} s^{-1}) can be used to estimate the time required for the brine to equilibrate with the atmosphere. For these calculations, the brine volume was determined by multiplying V_b/V by the 30 cm $\times$ 100 cm $\times$ 100 cm volume of ice (Table 4).

At the start of our study, we estimate a loss of 2.2 mmol CO_2 per m^2 per day from the upper ice (snow removed), indicating that the ice-atmosphere pCO_2 gradient would have been completely

Table 5. Main Factors Influencing Sea Ice pCO_2 Over the Spring Warming Period (Figure 13)

Sea Ice Zone	Early Warming	Advanced Warming
Snow-ice surface (upper ice)	Wind ventilation + packing (permeability)	Melt + re-freezing (permeability)
Middle-ice column	• Permeability • Dilution (in situ melt) • Solubility control (T, S)	• Dilution (in situ melt) • $CaCO_3$ dissolution + seawater mixing
Bottom ice	Biological CO_2 uptake	Biological CO_2 uptake
Dominant processes controlling sea ice (brine) pCO_2	Physical	Biogeochemical

(e.g., by snow or superimposed ice) or that significant CO_2 production occurred in situ to maintain high brine pCO_2 despite degassing. Measured flux from the overlying snow on 24 May was likewise positive and accounted for almost 70% of the flux from the upper ice (0.016 μmol m^{-2} s^{-1}; Figure 6b). To account for this efflux, while brine pCO_2 remained high, requires that CO_2 be produced at a similar rate (i.e., 10^{-2} μmol m^{-2} s^{-1}). Although we have no data available to estimate rates of bacterial C-respiration during our study, even the most generous estimates from Arctic spring sea ice are an order of magnitude lower than would be needed ($\approx$ 0.0064 μmol m^{-2} s^{-1}, using the highest average bottom ice measurements scaled to our 0.3 cm upper ice column thickness [*Nguyen and Maranger*, 2011]). At present, we cannot account for a scenario that would produce CO_2 within the ice or snow at such a rate, and therefore conclude that CO_2 diffusion from sea-ice brine to the atmosphere was impeded, despite likely high permeability (brine volume fraction >5%) [*Golden et al.*, 1998; *Pringle et al.*, 2009].

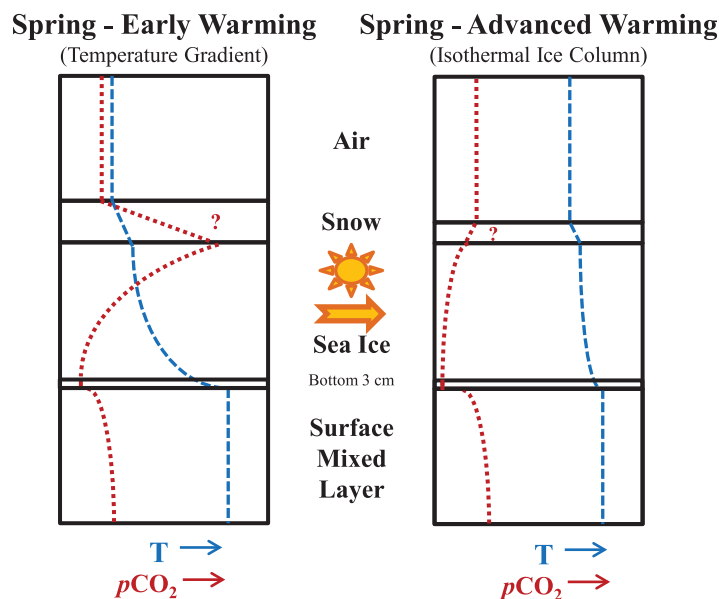eroded in less than half a day (9.5 h), if not otherwise impeded. However, bulk ice samples collected from the upper 10–30 cm 3 and 6 days later (27 May and 30 May) yielded average supersaturated brine pCO_2 values of 810 μatm and 1215 μatm, respectively (Figure 6a). This high supersaturation suggests either efflux from the ice to the atmosphere was restricted

Spring observations by *Fischer* [2013] the following year in Resolute Bay indicated that CO_2 fluxes were low or negligible through both snow cover and ice (with snow removed) in the early season (25 May to 3 June), despite high brine volume ($\approx$10%) and high brine pCO_2 (>800 ppm) in the upper ice. Sustained CO_2 efflux to the atmosphere was not observed over either surface until the ice column became isothermal (4 June until 10 June). As with our study, *Fischer* [2013] observed the largest CO_2 efflux events over ice with the snow cover removed, but these occurred much later in the seasonal development of the ice column than our observations. In our 2010 study, CO_2 efflux was measured while an obvious temperature gradient was still present in the ice column and the ice-snow interface was relatively cold ($\approx$ −4.5°C; cf. Figures 2a, 2c, 6b, and 6c).

Figure 13. Schematic illustration of the main factors influencing sea-ice pCO_2 over the spring warming period, as detailed in Table 5. Each plot illustrates vertical profiles of relative temperature (T) and pCO_2 from the air, through the snow and sea ice (with the bottom 3 cm emphasized), and into the underlying surface waters. The early spring period (left plot) is defined by strong temperature and pCO_2 gradients from the snow-ice to the ice-water interface; physical processes dominate measured brine pCO_2 during this period. As warming advances (right column), the temperature and pCO_2 gradients diminish over the ice column; physical processes are still important during this period, but biogeochemical processes (e.g., $CaCO_3$ dissolution and biological CO_2 uptake) begin to dominate measured brine pCO_2. Question marks "?" indicate our uncertainty in the pCO_2 gradient in snow layer, as observations over our time series suggest this interface is highly variable.

As air T increased, brine volume (and permeability) further increased in the upper ice, meaning bulk CO_2 diffusion would have to have been completely restricted on 30 May to account for the absence of an observable flux (Figure 6c) in the presence of a strong pCO_2 gradient (Table 4). Although we removed the snow before measuring the ice-air fluxes, refreezing of snow meltwater within the surface ice or the presence of low salinity ice from a previous melt event may have blocked gas exchange [*Eicken et al.*, 2002; *Polashenski et al.*, 2012]. Likewise, refreezing of melt water and the formation of ice lenses or superimposed ice within the snow cover can impede exchange between the snow and the atmosphere [*Zemmelink et al.*, 2006; *Nomura et al.*, 2010b]. Ice lenses within the snow cover were not observed at our field site until after 7 June, around the date when the snow surface began showing a consistently negligible CO_2 flux (Figure 6b).

After 30 May, the CO_2 sink into the snow-free sea ice surface strengthened (Figure 6c), whereas fluxes at the snow surface averaged around zero (Figure 6b). On our final time point in Table 4 (9 June), CO_2 uptake was measured at the ice surface (Figure 6c and Table 4), as pCO_2 in the upper ice became undersaturated with respect to the atmosphere (Figure 6a). This marked the transition from early season efflux to CO_2 uptake by the melting ice surface as warming advanced. Other studies have observed a similar transition between efflux and uptake over the spring season, and previous authors have attributed increased CO_2 absorption to snow melt dilution of the ice surface and the associated reduction in ice pCO_2 associated with internal ice melt [*Delille*, 2006; *Zemmelink et al.*, 2006; *Nomura et al.*, 2010a; *Geilfus et al.*, 2012]. Interestingly, *Fischer* [2013] did not observe such a clear transition from outgassing to uptake during his study in Allen Bay the following year. Although his high-temporal resolution flux measurements did identify some strong uptake events late in the season, these were interrupted by periods of efflux to the atmosphere.

As snow and internal ice melt began to dilute the ice surface with warming (Figure 2d), CO_2 uptake increased (Figure 6c). The transition to a completely isothermal ice column after 4 June (Figure 2c) was accompanied by undersaturation of pCO_2 within the remainder of the ice column (Figures 4g–4i). This transition toward pCO_2 under-saturation over the entire ice column would contribute to a weak CO_2 sink as melt advances, marking the end of the early melt period.

6. Conclusions

Observations over a 6 week time series of landfast sea ice in Resolute Passage captured an important transition over the early-melt period. We observed a spatial and temporal segregation between the dominant processes controlling CO_2 within the ice, distinguishing the bottom ice, the middle-ice column, and the upper ice/ice-atmosphere interface into separate biogeochemical zones, despite the high connectivity of the brine system in the warming ice (as summarized in Figure 13 and Table 5). Our time series illustrated that pCO_2 within the ice was strongly controlled by physical processes associated with warming. During the early warming period, sea ice melt dilution exerted a substantial influence on pCO_2 within the majority of the ice column, except in the bottom ice, where biological DIC uptake maintained undersaturated pCO_2 conditions throughout the time series. Although brine pCO_2 was primarily controlled by freshwater dilution, $CaCO_3$ dissolution appeared to have measurably reduced pCO_2 in the middle-ice column as warming advanced. In the upper ice, gas fluxes measured in the early season confirm that sea ice can act as a source of CO_2 to the atmosphere when brine pCO_2 is above atmospheric saturation. However, CO_2 diffusion appeared to be effectively impeded, enabling the persistence of a strong gradient favoring efflux, even as warming advanced. These observations suggest that the majority of the large pCO_2 reservoir retained in sea ice over winter is merely stored until spring, when freshwater dilution decreases pCO_2. Aside from CO_2 drawdown by photosynthetic algae in the bottom 3–10 cm of ice, brine pCO_2 in the majority of the ice column is controlled by solubility. Thus, the only net change in inorganic carbon inventory over the transition from winter to spring is associated with a small uptake of CO_2 due to $CaCO_3$ dissolution, likely balancing CO_2 redistribution during $CaCO_3$ formation in early winter.

The dissolution of $CaCO_3$ in melting sea ice, followed by the contribution of these high TA meltwaters to the surface ocean, has been observed to promote CO_2 uptake from the atmosphere over the melt season [e.g., *Geilfus et al.*, 2012]. *Rysgaard et al.* [2011] estimate that melting the entire volume of Arctic sea ice (8480 km^3) into a 50 m mixed layer would contribute to a net air-sea CO_2 flux of as much as -31 Tg C yr^{-1}, equivalent to almost 16% of the high latitude open ocean air-sea CO_2 flux [*Takahashi et al.*, 2009]. Making a similar calculation using data from this study (average sea ice, 10–110 cm: TA/TIC = 1.08, $S = 5$,

thickness = 140 cm; average seawater: TA/TIC = 1.04, S = 32.5, 50 m mixed layer), we estimate a much smaller net air-sea CO_2 flux of -7 Tg C yr^{-1} upon melting an equivalent volume of Arctic sea ice. The main reason for our lower estimate is the difference in the reported average TA/TIC of sea ice. In our study this value was very close to that of the underlying seawater, whereas *Rysgaard et al.* [2011] used a much higher ratio (1.80), leading to a larger change in TA/TIC, despite thinner sea ice (1.06 m). If the same calculation is carried out while maintaining seawater TA/TIC (i.e., sea ice TA/TIC =seawater TA/TIC), almost 80% of our estimated C uptake (-5.5 Tg C yr^{-1}) can be attributed to increased CO_2 solubility due to melt dilution alone. Our results suggest the impact of sea ice melt on the seasonal surface ocean CO_2 sink in the Arctic Ocean may be small, and that regional differences in the surface water inorganic carbon inventory may play a more significant role in determining the net effect of sea ice melt on the air-sea CO_2 flux. Furthermore, our results indicate that drainage of low TA:TIC brines, such as those we observed, triggered by early-spring warming would be an ineffective seasonal sea-ice carbonate pump, as early season brine TA:TIC differed only marginally from surface seawater in our study area.

Observations during this field study reveal a surprisingly dynamic carbon system within the sea ice, even before the snow had melted from the ice surface. Spatial segregation of abiotic and biotic processes during the early melt period create a heterogeneous, transitional environment in which the lower portion of the ice column can become sufficiently permeable and illuminated to support rapidly growing autotrophic communities, while the upper portion of the ice remains dominated by the physical constraints characterizing the late winter sea-ice system. Reduction of snow cover and the transition to a completely isothermal ice column mark the end of the early melt period and drive the ice column toward pCO$_2$ under-saturation, contributing to a weak CO_2 sink as melt advances. Future work during this dynamic period in the sea-ice life cycle should include combined studies of sea-ice physics (e.g., permeability, brine convection) and CO_2 gas transport across the entire ice column to better constrain exchanges through the ice itself, not just across its boundaries. Likewise, the determination of the isotopic fractionation factors for ikaite would permit the use of isotope mass balance studies as a powerful tool to determine carbon cycling within these systems. Furthermore, precise derivation of the stoichiometric equilibrium constants for the carbonic acid system in polar environments is needed before we can be truly confident in the use of calculated carbon system parameters in this environment.

References

Arrigo, K. R., T. Mock, and M. P. Lizotte (2010), Primary producers and sea ice, in *Sea Ice*, edited by D. N. Thomas and G. S. Dieckmann, pp. 283–325, Wiley-Blackwell, West Sussex, U. K.

Brown, K. A., L. A. Miller, M. Davelaar, R. Francois, and P. D. Tortell (2014), Over-determination of the carbonate system in natural sea-ice brine and assessment of carbonic acid dissocation constants under low temperature, high salinity conditions, *Mar. Chem.*, 165, 36–45, doi:10.1016/j.marchem.2014.07.005.

Carnat, G., T. Papakyriakou, N. X. Geilfus, F. Brabant, B. Delille, M. Vacoppenolle, G. Gilson, J. Zhou, and J. L. Tison (2013), Investigations on physical and textural properties of Arctic first-year sea ice in the Amundsen Gulf, Canada, November 2007–June 2008 (IPY-CLF system study), *J. Glaciol.*, 59(217), 819–837.

Chierici, M., A. Fransson, B. Lansard, L. A. Miller, A. Mucci, E. Shadwick, H. Thomas, J.-É. Tremblay, and T. N. Papakyriakou (2011), Impact of biogeochemical processes and environmental factors on the calcium carbonate saturation state in the Circumpolar Flaw Lead in the Amundsen Gulf, Arctic Ocean, *J. Geophys. Res.*, 116, C00G09, doi:10.1029/2011JC007184.

Cota, G. F., S. J. Prinsenberg, E. B. Bennet, J. W. Loder, M. R. Lewis, J. L. Anning, N. H. F. Watson, and L. R. Harris (1987), Nutrient fluxes during extended blooms of Arctic ice algae, *J. Geophys. Res.*, 92(C2), 1951–1962.

Cox, G. F. N., and W. F. Weeks (1983), Equations for determining the gas and brine volumes in sea ice samples, *J. Glaciol.*, 29(102), 306–316.

Delille, B. (2006), Inorganic carbon dynamics and air-ice-sea CO_2 fluxes in the open and coastal waters of the Southern Ocean, PhD thesis, 296 pp., Univ. de Liège, Liège, Belgium.

Delille, B., B. Jourdain, A. V. Borges, J.-L. Tison, and D. Delille (2007), Biogas (CO_2, O_2, dimethylsulfide) dynamics in spring Antarctic fast ice, *Limnol. Oceanogr. Methods*, 52(4), 1367–1379.

Deming, J. W. (2010), Sea ice bacteria and viruses, in *Sea Ice*, edited by D. N. Thomas and G. S. Dieckmann, pp. 247–282, Wiley-Blackwell, West Sussex, U. K.

Dickson, A. G. (1990), Standard potential of the reaction: AgCl(s) + 1/2H$_2$(g) = Ag (s) + HCl(aq), and and the standard acidity constant of the ion HSO$_4^-$ in synthetic sea water from 273.15 to 318.15 K, *J. Chem. Thermodyn.*, 22, 113–127.

Dickson, A. G., and F. J. Millero (1987), A comparison of the equilibrium constants for the dissociation of carbonic acid in seawater media, *Deep Sea Res., Part A*, 34(10), 1733–1743.

Dickson, A. G., C. L. Sabine, and J. R. Christian (Eds.) (2007), *Guide to Best Practices for Ocean CO$_2$ Measurements*, PICES Spec. Publ. 3, PICES, 191 pp.

Dieckmann, G. S., G. Nehrke, S. Papadimitriou, J. Göttlicher, R. Steininger, H. Kennedy, D. Wolf-Gladrow, and D. N. Thomas (2008), Calcium carbonate as ikaite crystals in Antarctic sea ice, *Geophys. Res. Lett.*, 35, L08501, doi:10.1029/2008GL033540.

Dieckmann, G. S., G. Nehrke, C. Uhlig, J. Göttlicher, S. Gerland, M. A. Granskog, and D. N. Thomas (2010), Ikaite (CaCO$_3$·6H$_2$O) discovered in Arctic sea ice, *Cryosphere*, 4(2), 227–230, doi:10.5194/tc-4-227-2010.

Else, B. G. T., T. N. Papkyriakou, R. Raddatz, R. J. Galley, C. J. Mundy, D. G. Barber, K. Swystun, and S. Rysgaard (2014), Surface energy budget of landfast sea ice during the transitions from winter to snowmelt and melt pond onset: The importance of net longwave radiation and cyclone forcings, *J. Geophys. Res. Oceans*, 119, 3679–3693, doi:10.1002/2013JC009672.

Eicken, H., H. R. Krouse, D. Kadko, and D. K. Perovich (2002), Tracer studies of pathways and rates of meltwater transport through Arctic summer sea ice, *J. Geophys. Res.*, *107*(C10), 8046, doi:10.1029/2000JC000583.

Fransson, A., M. Chierici, L. A. Miller, G. Carnat, E. Shadwick, H. Thomas, S. Pineault, and T. N. Papapkyriakou (2013), Impact of sea-ice processes on the carbonate system and ocean acidification at the ice-water interface of the Amundsen Gulf, Arctic Ocean, *J. Geophys. Res. Oceans*, *118*, 7001–7023, doi:10.1002/2013JC009164.

Fischer, M. (2013), Sea ice and the air-sea exchange of CO_2, PhD thesis, 219 pp., Bremen Univ., Bremen, Germany.

Galindo, V., M. Levasseur, C. J. Mundy, M. Gosselin, J.-É. Tremblay, M. Scarratt, Y. Gratton, T. Papakiriakou, M. Poulin, and M. Lizotte (2014), Biological and physical processes influencing sea ice, under-ice algae, and dimethylsulfoniopropionate during spring in the Canadian Arctic Archipelago, *J. Geophys. Res. Oceans*, *119*, 3746–3766, doi:10.1002/2013JC009497.

Geilfus, N.-X., G. Carnat, T. Papakyriakou, J.-L. Tison, B. Else, H. Thomas, E. H. Shadwick, and B. Delille (2012), Dynamics of pCO_2 and related air-ice CO_2 fluxes in the Arctic coastal zone (Amundsen Gulf, Beaufort Sea), *J. Geophys. Res.*, *117*, C00G10, doi:10.1029/2011JC007118.

Gleitz, M., M. Rutgers, V. D. Leoff, D. N. Thomas, G. S. Dieckmann, and F. J. Millero (1995), Comparison of summer and winter inorganic carbon, oxygen and nutrient concentrations in Antarctic sea ice brine, *Mar. Chem.*, *51*, 81–91.

Golden, K. M., S. F. Ackley, and V. I. Lytle (1998), The percolation phase transition in sea ice, *Science*, *282*, 2238–2241, doi:10.1126/science.282.5397.2238.

Gosselin, M., L. Legendre, S. Demers, and R. G. Ingram (1985), Responses of sea-ice microalgae to climatic and fortnightly tidal energy inputs (Manitounuk Sound, Hudson Bay), *Can. J. Fish. Aquat. Sci.*, *42*, 999–1006.

IUPAC (1997), *Compendium of Chemical Terminology*, 2nd ed., edited by A. D. McNaught and A. Wilkinson, Blackwell Sci., Oxford, U. K., doi:10.1351/goldbook.P04758. [Available at http://goldbook.iupac.org.]

Jones, E. P., and A. R. Coote (1981), Oceanic CO_2 produced by the precipitation of $CaCO_3$ from brines in sea ice, *J. Geophys. Res.*, *86*(C11), 11,041–11,043.

Kennedy, H., D. N. Thomas, G. Kattner, C. Haas, and G. S. Dieckmann (2002), Particulate organic matter in Antarctic summer sea ice : Concentration and stable isotopic composition, *Mar. Ecol. Prog. Ser.*, *238*, 1–13.

Leppäranta, M., and T. Manninen (1988), The brine and gas content of sea ice with attention to low salinities and high temperatures, *Finn. Inst. Mar. Res. Internal Rep. 1988-2*, 15 pp., Finn. Inst. of Mar. Res., Helsinki, Finland.

Loose, B., L. A. Miller, S. Elliot, and T. Papakyriakou (2011), Sea ice biogeochemistry and material transport across the frozen interface, *Oceanography*, *24*(3), 202–218, doi:10.5670/oceanog.2011.72.

McLaughlin, F. A., et al. (2012), Physical, chemical and zooplankton data from the Canada Basin and Canadian Arctic Archipelago, July 20 to September 14, 2006, *Can. Data Rep. Hydrogr. Ocean Sci. 186*, x + 373 pp.

Mehrbach, C., C. H. Culberson, J. E. Hawley, and R. M. Pytkowicz (1973), Measurement of the apparent dissociation constants of carbonic acid in seawater at atmospheric pressure, *Limnol. Oceanogr.*, *18*(6), 897–907.

Melling, H., T. A. Agnew, K. K. Falkner, D. A. Greenberg, C. M. Lee, A. Munchow, B. Petrie, S. J. Prinsenberg, R. M. Samelson, and R. A. Woodgate (2008), Fresh-water fluxes via Pacific and Arctic outflows across the Canadian Polar Shelf, in *Arctic-Subarctic Ocean Fluxes*, edited by R. R. Dickson, J. Meincke, and P. Rhines, pp. 193–247, Springer, Dordrecht, Netherlands.

Miller, L. A., G. Carnat, B. G. T. Else, N. Sutherland, and T. N. Papakyriakou (2011a), Carbonate system evolution at the Arctic Ocean surface during autumn freeze-up, *J. Geophys. Res.*, *116*, C00G04, doi:10.1029/2011JC007143.

Miller, L. A., T. N. Papakyriakou, R. E. Collins, J. W. Deming, J. K. Ehn, R. W. Macdonald, A. Mucci, O. Owens, M. Raudsepp, and N. Sutherland (2011b), Carbon dynamics in sea ice: A winter flux time series, *J. Geophys. Res.*, *116*, C02028, doi:10.1029/2009JC006058.

Mundy, C. J., M. Gosselin, Y. Gratton, K. A. Brown, V. Galindo, K. Campbell, M. Levasseur, D. Barber, and T. Papakyriakou (2014), The role of environmental factors on under-ice phytoplankton bloom initiation: A case study on landfast sea ice in Resolute Passage, Canada, *Mar. Ecol. Prog. Ser.*, *497*, 39–49, doi:10.3354/meps10587.

Munro, D. R., R. B. Dunbar, D. A. Mucciarone, K. R. Arrigo, and M. C. Long (2010), Stable isotope composition of dissolved inorganic carbon and particulate organic carbon in sea ice from the Ross Sea, Antarctica, *J. Geophys. Res.*, *115*, C09005, doi:10.1029/2009JC005661.

Nguyen, D., and R. Maranger (2011), Respiration and bacterial carbon dynamics in Arctic sea ice, *Polar Biol.*, *34*(12), 1843–1855, doi:10.1007/s00300-011-1040-z.

Niemi, A., C. Michel, K. Hille, and M. Poulin (2011), Protist assemblages in winter sea ice: Setting the stage for the spring ice algal bloom, *Polar Biol.*, *34*(12), 1803–1817, doi:10.1007/s00300-011-1059-1.

Nomura, D., H. Yoshikawa-Inoue, and T. Toyota (2006), The effect of sea-ice growth on air-sea CO_2 flux in a tank experiment, *Tellus, Ser. B*, *58*(5), 418–426, doi:10.1111/j.1600-0889.2006.00204.x.

Nomura, D., H. Eicken, R. Gradinger, and K. Shirasawa (2010a), Rapid physically driven inversion of the air–sea ice CO_2 flux in the seasonal landfast ice off Barrow, Alaska after onset of surface melt, *Cont. Shelf Res.*, *30*(19), 1998–2004, doi:10.1016/j.csr.2010.09.014.

Nomura, D., H. Yoshikawa-Inoue, T. Toyota, and K. Shirasawa (2010b), Effects of snow, snowmelting and refreezing processes on air–sea-ice CO_2 flux, *J. Glaciol.*, *56*(196), 262–270, doi:10.3189/002214310791968548.

Nomura, D., P. Assmy, G. Nehrke, M. A. Granskog, M. Fischer, G. S. Dieckmann, A. Fransson, Y. Hu, and B. Schnetger (2013a), Characterization of ikaite ($CaCO_3 \cdot 6H_2O$) crystals in first-year Arctic sea ice north of Svalbard, *Ann. Glaciol.*, *54*(62), 125–131, doi:10.3189/2013AoG62A034.

Nomura, D., M. A. Ganskog, P. Assmy, D. Simizu, and G. Hasida (2013b), Arctic and Antarctic sea ice acts as a sink for atmospheric CO_2 during peroids of snowmelt and surface flooding, *J. Geophys. Res. Oceans*, *118*, 6511–6524, doi:10.1002/2013JC009048.

Papadimitriou, S., H. Kennedy, G. Kattner, G. S. Dieckmann, and D. N. Thomas (2004), Experimental evidence for carbonate precipitation and CO_2 degassing during sea ice formation, *Geochim. Cosmochim. Acta*, *68*(8), 1749–1761, doi:10.1016/j.gca.2003.07.004.

Papadimitriou, S., D. N. Thomas, H. Kennedy, C. Haas, H. Kuosa, A. Krell, and G. S. Dieckmann (2007), Biogeochemical composition of natural sea ice brines from the Weddell Sea during early austral summer, *Limnol. Oceanogr. Methods*, *52*(5), 1809–1823.

Papadimitriou, S., D. Thomas, H. Kennedy, H. Kuosa, and G. Dieckmann (2009), Inorganic carbon removal and isotopic enrichment in Antarctic sea ice gap layers during early austral summer, *Mar. Ecol. Prog. Ser.*, *386*, 15–27, doi:10.3354/meps08049.

Papadimitriou, S., H. Kennedy, L. Norman, D. P. Kennedy, G. S. Dieckmann, and D. N. Thomas (2012), The effect of biological activity, $CaCO_3$ mineral dynamics, and CO_2 degassing in the inorganic carbon cycle in sea ice in late winter-early spring in the Weddell Sea, Antarctica, *J. Geophys. Res.*, *117*, C08011, doi:10.1029/2012JC008058.

Papakyriakou, T., and L. A. Miller (2011), Springtime CO_2 exchange over seasonal sea ice in the Canadian Arctic Archipelago, *Ann. Glaciol.*, *52*(57), 215–224, doi:10.3189/172756411795931534.

Petrich, C., and H. Eicken (2010), Growth, structure and properties of sea ice, in *Sea Ice*, edited by D. N. Thomas and G. S. Dieckmann, pp. 23–78, Wiley-Blackwell, West Sussex, U. K.

Pierrot, D., E. Lewis, and D. W. R. Wallace (2006), MS Excel program developed for CO_2 system calculations, *ORNL/CDIAC-105a*, Carbon Dioxide Inf. Anal. Cent., Oak Ridge Natl. Lab., U.S. Dep. of Energy, Oak Ridge, Tenn., doi:10.3334/CDIAC/otg.CO2SYS_XLS_CDIAC105a.

Pringle, D. J., J. E. Miner, H. Eicken, and K. M. Golden (2009), Pore space percolation in sea ice single crystals, *J. Geophys. Res.*, *114*, C12017, doi:10.1029/2008JC005145.

Polashenski, C., D. Perovich, and Z. Courville (2012), The mechanisms of sea ice melt pond formation and evolution, *J. Geophys. Res.*, *117*, C01001, doi:10.1029/2011JC007231.

Rysgaard, S., R. N. Glud, M. K. Sejr, J. Bendtsen, and P. B. Christensen (2007), Inorganic carbon transport during sea ice growth and decay: A carbon pump in polar seas, *J. Geophys. Res.*, *112*, C03016, doi:10.1029/2006JC003572.

Rysgaard, S., J. Bendtsen, L. T. Pedersen, H. Ramløv, and R. N. Glud (2009), Increased CO_2 uptake due to sea ice growth and decay in the Nordic Seas, *J. Geophys. Res.*, *114*, C09011, doi:10.1029/2008JC005088.

Rysgaard, S., J. Bendtsen, B. Delille, G. S. Dieckmann, R. N. Glud, H. Kennedy, J. Mortensen, S. Papadimitriou, D. N. Thomas, and J.-L. Tison (2011), Sea ice contribution to the air-sea CO_2 exchange in the Arctic and Southern Oceans, *Tellus, Ser. B*, *63*(5), 823–830, doi:10.1111/j.1600-0889.2011.00571.x.

Rysgaard, S.,et al. (2013), Ikaite crystal distribution in winter sea ice and implications for CO_2 system dynamics, *Cryosphere*, *7*(2), 707–718, doi:10.5194/tc-7-707-2013.

Schlitzer, R. (2012), Ocean Data View. [Available at http://odv.awi.de.]

Semiletov, I. P., A. Makshtas, and S.-I. Akasofu (2004), Atmospheric CO_2 balance: The role of Arctic sea ice, *Geophys. Res. Lett.*, *31*, L05121, doi:10.1029/2003GL017996.

Shirasawa, K., and R. G. Ingram (1997), Currents and turbulent fluxes under the first-year sea ice in Resolute Passage, Northwest Territories, Canada, *J. Mar. Syst.*, *11*, 21–32.

Takahashi, T., et al. (2009), Climatological mean and decadal change in surface ocean pCO_2, and net sea–air CO_2 flux over the global oceans, *Deep Sea Res., Part II*, *56*, 554–577.

Thomas, D. N., S. Papadimitriou, and C. Michel (2010), Biogeochemistry of sea ice, in *Sea Ice*, edited by D. N. Thomas and G. S. Dieckmann, pp. 425–467, Wiley-Blackwell, West Sussex, U. K.

Toyota, T., I. J. Smith, A. J. Gough, P. J. Langhorne, G. H. Leonard, R. J. Van Hale, A. R. Mahoney, and T. G. Haskell (2013), Oxygen isotope fractionation during the freezing of sea water, *J. Glaciol.*, *59*, 697–710. doi:10.3189/2013JoG12J163.

Vancoppenolle, M., H. Goosse, A. de Montety, T. Fichefet, B. Tremblay, and J.-L. Tison (2010), Modeling brine and nutrient dynamics in Antarctic sea ice : The case of dissolved silica, *J. Geophys. Res.*, *115*, C02005, doi:10.1029/2009JC005369.

Weiss, R. F., and B. A. Price (1980), Nitrous oxide solubility in water and seawater, *Mar. Chem.*, *8*(4), 347–359, doi:10.1016/0304-4203(80)90024-9.

Zeebe, R. E., and D. Wolf-Gladrow (2001), *CO_2 in Seawater: Equilibrium, Kinetics, Isotopes, Elsevier Oceanogr. Ser. 65*, Elsevier Ltd., San Diego, Calif.

Zemmelink, H. J., B. Delille, J. L. Tison, E. J. Hintsa, L. Houghton, and J. W. H. Dacey (2006), CO_2 deposition over the multi-year ice of the western Weddell Sea, *Geophys. Res. Lett.*, *33*, L13606, doi:10.1029/2006GL026320.

Zhou, J., B. Delille, H. Eicken, M. Vancoppenolle, F. Brabant, G. Carnat, N.-X. Geilfus, T. Papakyriakou, B. Heinesch, and J.-L. Tison (2013), Physical and biogeochemical properties in landfast sea ice (Barrow, Alaska): Insights on brine and gas dynamics across seasons, *J. Geophys. Res. Oceans*, *118*, 3172–3189, doi:10.1002/jgrc.20232.